# How well does an Earth System Model represent the occlusion of extratropical cyclones?

Catherine M Naud,[a] Gregory S Elsaesser,[a] Poushali Ghosh,[b] Jonathan E Martin,[b] and Derek J Posselt[c]

[a] *Applied Physics and Applied Mathematics, Columbia University/NASA GISS, New York, NY*

[b] *Atmospheric and Oceanic Sciences, University of Wisconsin-Madison, Madison, WI*

[c] *Jet Propulsion Laboratory, California Institute of Technology, Pasadena, CA*

*Corresponding author*: Catherine Naud, cn2140@columbia.edu

ABSTRACT

Extratropical cyclones are the main providers of midlatitude precipitation. How extratropical cyclones will change in a warming climate is unclear, thus leading to uncertainty in simulated midlatitude precipitation changes. The latest NASA Goddard Institute for Space Studies (GISS) Earth System models (ESMs) accurately simulate the location and structure of cyclones, though deficiencies in cyclone cloud and precipitation simulation are found. To provide a new process-level context for evaluation of midlatitude-simulated cloud and precipitation, occluded cyclones are examined. Occlusions involve the formation of a thermal ridge, maintained via latent heat release in the wider three-dimensional TROWAL region. Using a novel method for objective identification of occluded cyclones, the simulation of occlusion in the latest GISS-E3 model is examined. The model produces occluded cyclones, but less frequently than observed, and shifted poleward and towards the exit region of the climatological storm tracks. Nevertheless, E3 reproduces adequately the thermal and kinematic structure of the thermal ridge, with realistic depth and poleward tilt. Compared to CloudSat-CALIPSO cloud retrievals across the thermal ridge, the dependence of cloud properties on thermal ridge strength is well represented, though at the expense of producing low ice mass clouds too often at high altitudes (i.e. “too many, too tenuous”). Overall, E3 shows clear improvements from its predecessor, highlighting the value of improved cloud parameterizations. E3 produces significantly more precipitation in occluded versus non-occluded cyclones, demonstrating the importance of accurately representing occlusions and associated hydrological processes in ESMs.

## 1. Introduction

The majority of the precipitation in the mid-latitudes (30°-60°N/S) is delivered by extratropical cyclones and their attendant fronts, up to 80% in the winter (Hawcroft et al., 2012; Catto et al., 2012). These systems are also responsible for the most extreme of precipitation events (Pfahl and Wernli, 2012; Kunkel et al., 2012). As the Earth’s climate changes, concurrent changes in extratropical cyclones, their attendant precipitation distributions, as well as associated extremes are the subject of active research (e.g. Bengtsson et al., 2009; Pfahl and Wernli, 2012; Kunkel et al., 2013; Marciano et al. 2015). Future climate predictions suggest an increase in the precipitation associated with extratropical cyclones (Zhang and Colle, 2018), forced by changes in temperature and moisture availability (Yettella and Kay, 2017), but not so

much by changes in cyclone strength (Sinclair and Catto, 2023). Baroclinicity may be expected to decrease because of a reduced temperature gradient in the lower troposphere. However, this might be compensated by an increase in temperature gradient in the upper troposphere (Sinclair and Catto, 2023). In addition, many studies have shown the importance of latent heat release in areas of cloud and precipitation formation for cyclone development (Binder et al., 2016), but cloud and precipitation representation, and their associated latent heating, in Earth System Models (ESMs) are still deficient (e.g. Catto et al., 2015; Naud et al., 2020). Therefore, the ESM representation of moist processes associated with extratropical cyclones needs to be further evaluated to increase confidence in future climate predictions.

One aspect of the cyclone life cycle that is strongly influenced by latent heat release is the occlusion process, whereby cyclones adopt a characteristic thermal structure as they reach their post-mature phase. First introduced by Bergeron (Jewell, 1981), the warm occlusion process involves the cold front encroaching upon, and eventually ascending, the warm frontal surface, which promotes the production of a wedge of warm air aloft displaced poleward of the warm front. This warm wedge manifests as a thermal ridge between the cyclone center and the peak of the warm sector (Martin, 1998a,b, 1999a,b; Schultz and Vaughan, 2011 and references therein). Warm moist air is forced to ascend cyclonically from the warm sector boundary layer through the thermal ridge, predominantly via positive vorticity advection by the thermal wind (Sutcliffe, 1947; Martin 1999a,b), filling a sloping three-dimensional region called the Trough of Warm air Aloft or TROWAL (Crocker et al., 1947; Penner, 1955) with clouds and precipitation. It is this region of the cyclone, not along the surface occluded front, where some of the heaviest precipitation observed in the occluded cyclone often occurs (Grim et al, 2007; Han et al. 2007; Martin, 1998b; Naud et al., 2024). Therefore, the occluded thermal ridge (OTR) is the location of substantial latent heat release which, in turn, substantially shapes the tropopause-level potential vorticity (PV) and tropospheric thermal structure of the canonical warm occlusion (Posselt and Martin, 2004). Thus, examination of the structure and evolution of occluded cyclones in an ESM indirectly contributes to evaluation of the model's fidelity in representing latent heat release and its impacts.

To the authors' knowledge there have been no prior studies that document the occurrence, the structure or the evolution of occluded cyclones in ESMs. This is partly because, until recently, there was no automated method to identify occlusions in models. In Naud et al. (2023), such a method was designed and applied to the Modern Era retrospective analysis for research and applications version 2 (MERRA-2; Gelaro et al., 2017). The same method can be applied to any gridded dataset, observational or otherwise, thus making it suitable for application to models, enabling novel process-level model evaluation. In this study, we apply the identification methodology to the Goddard Institute for Space Studies (GISS) latest Earth system model (GISS-E3). Using MERRA-2 and combined observations from CloudSat (Stephens et al. 2002) and CALIPSO (Winker et al. 2007) for reference, we evaluate E3's ability to represent occlusions, their structure, and their cloud properties in the OTR. This analysis is aimed at addressing the following questions: 1) Does an ESM represent the occlusion process?, 2) How well does it represent the thermal, kinematic and cloud structure of the occluded cyclone?, and 3) How does an examination of occluded cyclones assist in identifying potential model deficiencies?

The examination of these questions is organized as follows. Section 2 presents details concerning the model and its integration, the datasets used for comparison, as well as the various tools needed for the intended analysis. The evaluation of the model's depiction of occlusions is detailed in section 3 and progresses from examination of the large-scale environment within which the storms form to the cyclone scale and then finally to the thermal ridge scale. Section 4 includes a discussion on the progress made in E3 compared to the earlier CMIP6 version of the GISS model (E2.1; Kelley et al., 2020). Here we also consider why and how an accurate representation of occlusions in E3 informs understanding of the model's depiction of precipitation distribution as well as extremes. A summary and conclusions are available in section 5.

## 2. Model, datasets and methodology

This section describes the model to be tested, the datasets used for the subsequent analysis as well as the various algorithms and tools employed throughout the analysis.

*a. The CMIP6 NASA Goddard Institute for Space Studies Earth System Model*

GISS-E3, the latest and most advanced of three GISS contributions to CMIP6, is the focus of this study. E3 comprises substantial upgrades to multiple physics parameterizations, an increase in vertical resolution (from 40 to 110 layers), and use of a machine learning algorithm to more objectively calibrate or "tune" (Schmidt et al. 2017) the ESM. An early summary of the physics upgrades relative to E2.1 is available in Cesana et al. (2019), with the particular tuned candidate known as "Tun2" analyzed in this study (Cesana et al. 2021, Li et al. 2023). A selection of the pertinent physics upgrades that directly affect cloud and precipitation are summarized below:

- New Planetary Boundary Layer (PBL) physics that includes novel heat flux equations without use of a critical Richardson number is implemented into GISS-E3 (Cheng et al. 2020), along with a new moist turbulence scheme based on Bretherton and Park (2009).
- Improvements in convective macrophysics (e.g., cold pool impact on convection; Del Genio et al. 2015) and microphysics (Elsaesser et al. 2017a) have led to improved representation of convective clouds and the transition from shallow to deep convection.
- Prognostic stratiform precipitation (MG2 microphysics; Gettelman and Morrison 2015) and a new stratiform cloud fraction scheme (Smith 1990).

In GISS-E3, ice water path (IWP) and liquid water path (LWP) are substantially decreased from previous versions of the model, and in closer agreement with observational estimates (Elsaesser et al. 2017a, b). Substantial improvments in simulating convective phenomena are also noted (e.g., tropical cyclones; Russotto et al. 2022). The current analysis utilizes an atmosphere-only free-running integration of E3, forced with prescribed transient monthly varying sea surface temperaures. Our focus is on the 2006 – 2011 period, which overlaps with the first five years of the CloudSat/CALIPSO mission. We use the 2.5°x2° horizontal resolution configuration as in Cesana et al. (2019), Cesana et al. (2021), and Li et al. (2023), even though c90 ( ~1°) resolution will be the final resolution submitted to CMIP6. Model data, available at 3-hourly temporal resolution, includes: two-dimensional sea-level pressure and surface precipitation, and profiles (on 110 vertical levels from 979 to 0.0035 hPa) of temperature, specific humidity, geopotential height, wind, vertical velocity, cloud fraction, ice and liquid water content for both suspended and falling condensate. We also perform a cursory evaluation of

the occlusion structure in the GISS-E2.1 model (same horizontal resolution, but substantially different cloud parameterizations; full details in Kelley et al., 2020) so as to infer what magnitude of change might be expected in occlusion structure representation upon a typical increase in vertical resolution and advancement in cloud parameterization across a CMIP generation.

### *b. MERRA-2 and CloudSat-CALIPSO for Reference Datasets*

To evaluate the performance of E3, we use the Modern Era Retrospective Analysis for Research and Applications version 2 (MERRA-2; Gelaro et al., 2017) environmental variables, including profiles of geopotential height, temperature, wind, specific humidity and vertical velocity. The cyclone tracking database is described in the next section. The CloudSat-CALIPSO GEOPROF-LIDAR (Mace et al., 2008; Mace and Zhang, 2014) and 2C-ICE (Deng et al. 2010) products serve as the sources for observed cloud hydrometeor states in cyclones.

The GEOPROF-LIDAR product combines hydrometeor identifications from both the radar and lidar and provides the location of up to five cloud layer base and top heights in the CloudSat footprint (~1.3 km x 1.7 km). However, because CloudSat cannot distinguish falling from suspended particles, these cloud layers are more appropriately termed “hydrometeor layers”. We use the altitude information on cloud layer bases and tops to create a vertical profile of hydrometeor presence, which indicates whether cloud and/or precipitation are present at 250 m resolution in the vertical.

The 2C-ICE product provides ice water content profiles obtained using both lidar 532 nm attenuated backscatter and radar reflectivity profiles ingested into an optimal estimation algorithm. These profiles are provided at the resolution of the the CloudSat horizontal footprint (1.4 km across x 1.7 km along track). The uncertainty in retrieved IWC is estimated to be less than 30% (Deng et al., 2013), although that estimate might be substantially larger in precipitating clouds and with inceasing convective core vertical depth (i.e., in the tropics). The reported IWC has a minimum threshold that is dictated by both limits in lidar and radar detectability. However, the model does not have such limitations and will provide very small values of IWC that are currently unobservable. To ensure a fairer comparison, we define a minimum IWC for use in E3 evaluation that best matches the retrieval capability. For this, we

constructed a temperature dependent threshold on IWC based on a 10-granule collection of 2C-ICE retrievals, informed by data analysis provided by Deng (personal communication). The threshold ($IWC_{min}$) is computed as follows:

$$IWC_{min}=10^{-3.26474} \text{ where } T \leq 210K$$

$$IWC_{min}= 10^{((T-276.543)/20.3823)} \text{ where } T > 210 K$$

Where T is the temperature of each model grid cell level. The E3 IWC is set to zero in any grid cell level where $IWC(T) < IWC_{min}$. Tests reveal a notable difference in mean IWC without incorporation of thresholding, with E3 estimates closer to observations upon application of the threshold.

### *c. Tracking extratropical cyclones*

To identify the location of extratropical cyclones and track their evolution in time, we use the cyclone tracker algorithm of Bauer and Del Genio (2006). This algorithm utilizes gridded sea level pressure fields and searches for local minima. The algorithm is fully described and evaluated in Bauer et al. (2016). To briefly summarize, the algorithm first imposes thresholds for the central pressure and the difference in pressure relative to the surrounding area to decide whether the identified minima are indeed depressions. Upon identification, the candidate centers are tracked in time, with a number of thresholds imposed for the rate of change in central pressure and its maximum horizontal displacement. At the end, a list of cyclone tracks lasting at least 36 hours is generated, with information on the latitude and longitude of the cyclone center every 6 hours from cyclone intiation to dissipation. This algorithm was applied and tested by Bauer et al. (2016) on the ERA-Interim reanalysis (Dee et al., 2011). This ERA-interim based database is the cyclone location reference dataset used for evaluation of the GISS models. The same tracking algorithm is applied to the GISS model sea level pressure fields, with cyclone information stored every 6 hours for consistency.

### *d. Identification of occlusions*

Using the cyclone track climatology obtained with the Bauer and Del Genio method, an occlusion identification algorithm, as described in Naud et al. (2023), is then applied. The algorithm searches for cyclones with an occluded thermal ridge, which is a two-dimensional

projection of the full three-dimensional TROWAL region. The thermal ridge is identified around each cyclone center (within ±20° latitude, from 10° west to 20°east) by assessing the divergence of the unit vector of 1000-500 hPa thickness gradient ($\hat{n} = \frac{\nabla \emptyset'}{|\nabla \emptyset'|}$). The grid cells around the cyclone that 1) indicate convergence, and 2) are not in regions of heterogenous topography, are flagged and are tracked in time in a cyclone-centered grid through the cyclone life. If these converging regions overlap in time using this reference grid for at least two consecutive 6-hour time steps, and the period over which the overlap occurs contains or follows the time of maximum cyclone intensity (i.e. minimum in sea level pressure at the center over the entire lifetime), the cyclone is flagged as being occluded. Using MERRA-2, a database was produced for the period 2006-2017 that provides the list of cyclone instances that are occluded as well as the location of the thermal ridge. This is the publicly-available database serving as our observational compositing reference. The same algorithm is applied to Model E3, which further takes into account the coarser spatial resolution of the model (c.f. Naud et al., 2023).

*e. Compositing Methodology*

To facilitate comparison between the GISS models, MERRA-2 and the CloudSat/CALIPSO data, we developed a compositing methodology that enables dataset comparison and provides useful insight on occlusion characteristics (Naud et al., 2023; 2024). Two types of geometric reference frames are used: one that considers the cyclone as a whole and uses the cyclone center as an anchor for averaging various fields around the cyclone center and another that focuses on vertical transects across the thermal ridge.

For the cyclone-centered composites, the gridded fields are first projected onto a rectangular grid with south-north and west-east directions expressed in distance from the cyclone center, centered on the point of minimum in sea-level pressure with maximum dimensions ±4000 km west-east and ±3000 km south-north. The re-gridded fields from each cyclone are then superimposed before calculating the mean of all cyclones.

For the vertical transect composites, the thermal ridge serves as the anchor. The algorithm described in Section 2d identifies the thermal ridge in each occluded cyclone as a set of contiguous points at which $\nabla \cdot \hat{n}$ is smaller than a threshold value. A regression line (in

latitude/longitude) is then calculated through this cluster. This line represents the orientation of the thermal ridge axis. At the median longitude of this thermal ridge axis a transect line is drawn perpendicular to it. Finally, the thermal ridge axis line is slid along the transect line until it reaches the coincident 700 hPa $\theta_e$ maximum (hereafter referred to as max($\theta_e$)). The location of this maximum is the anchor for the composites (see Naud et al., 2023 for additional details). We find that max($\theta_e$) is the quantity that best describes the depth of the thermal ridge (Naud et al., 2023), and thus we use it throughout as a metric to characterize the ridges.

For MERRA-2 and the GISS models, geopotential heights, $\theta_e$ and vertical velocity profiles - and, for E3 only, cloud fraction and IWC profiles - are aggregated along the perpendicular line using a nearest neighbor approach and arranged into distance bins of 200 km width from 1500 km on the equator-west side of the ridge to 1500 km on its polar-east side. Using the location of max($\theta_e$) at 700 hPa as the zero point, the perpendicular transects of all the cyclones/thermal ridges are superimposed and their average calculated.

For the composite transects that involve use of the CloudSat-CALIPSO retrievals, the method has to be altered since the orbits provide data in random locations around the thermal ridges instead of along the perpendicular to the ridge at the median longitude. A full description of the approach adopted is available in Naud et al. (2024, see their Figure 2). In this case, all observational profiles (i.e., hydrometeor masks, ice water mass) in a broader region are used, as long as they are located between the two perpendiculars at the ridge extremities within $\pm$1500 km of any point along the ridge. In this case, the closest point along the ridge to each observed profile is used as the anchor to obtain the distance information needed to populate the transects. The effect of this random sampling of the entire ridge area as opposed to a simple perpendicular at the median longitude along the ridge was tested in Naud et al. (2024), and good agreement was found when this was applied to MERRA-2 $\theta_e$ profiles (c.f. their Figure 3).

## 3. Evaluation of occlusions in model E3

Because of topography, both cyclone tracking and occlusion identification algorithms may yield artifacts and result in larger uncertainties over land. Therefore, this study only considers cyclones whose centers reside over *open ocean*. For the analysis of occlusions in E3, we first

focus on the Northern Hemisphere (NH) winter season (December, January and February) for the 5-year period of 2006-2011. This hemisphere and season have been the foci of active research on occlusions, so there is ample literature providing additional references. This first part of the evaluation is performed using MERRA-2 for the comparison of all environmental variables. The latter part focuses on the thermal ridge, and for this we include hydrometeor retrievals from the combined CloudSat-CALIPSO products described above. For that part of the analysis, we expand the comparison to include both hemispheres and all seasons to allow better sampling.

*a. Are there occluded cyclones in E3?*

As discussed in Section 2.a, the Model E3 integration is performed using prescribed sea surface temperatures (free-running, with no nudging). Therefore, the cyclones that emerge in the model are not expected to match, in time and space, those that occurred in the real world. However, since the simulated climate resembles the real world climatology, extratropical cyclones are expected to collectively occur in places and at times that are comparable to reanalysis datasets. The first step, as a result, is to examine how closely the storm track and climate of E3 match those obtained with ERA-Interim/MERRA-2 for the same period of time.

Cyclones tend to congregate in regions referred to as the storm tracks (e.g. Hoskins and Hodges, 2002, for the NH), which are typically found between Japan and Alaska in the north Pacific basin and between the US Carolina coastline and Norway in the Atlantic ocean. The ERA-Interim reanalysis indicates two hot spots for the 2006-2011 winters (Figure 1a): one off the east coast of southern Greenland and another along the Alaskan south coast. Model E3 represents the location of the NH winter storm tracks realistically (Figure 1b). The total number of cyclones is close to that observed, but E3 1) tends to have more cyclones occurring near the exit of the Atlantic storm track than the reanalysis, 2) does not produce sufficient cyclones along the coast of Alaska and 3) produces too many along the entire southern coast of Greenland. Overall, the preferred storm locations in the model's Atlantic basin tend to be found poleward of those in the reanalysis. This is consistent with the differences in the upper- level jet, expressed as the mean zonal wind at 250 hPa in Fig. 1c. While differences are relatively small in

the Pacific ocean, the E3 north Atlantic jet is poleward of the reanalysis location, and expands further north-eastward than typically observed.

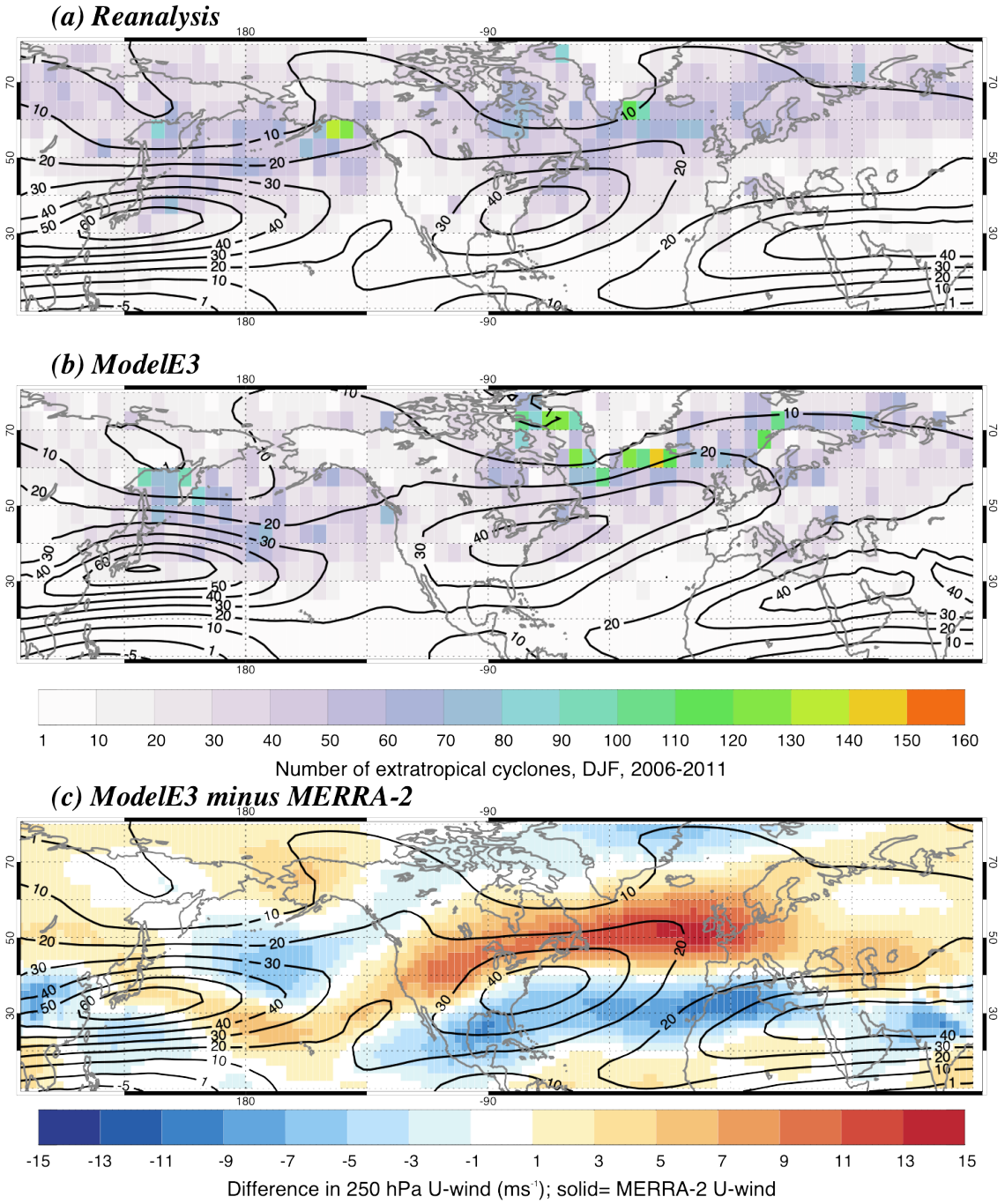


Figure 1: Number of extratropical cyclone centers in 5ºx5º regions (color, from 1 to 160 in increments of 10), that occurred in December, January and February 2006-2011 in (a) ERA-Interim and (b) ModelE3, with black contours showing the corresponding zonal wind speed at 250 hPa (from 1 to 60 m/s, every 10 m/s). (c) the difference in 250hPa zonal wind between

Model E3 and MERRA-2 for the same period. The black solid contour in (c) show the 250 hPa MERRA-2 zonal wind, in 1-m/s increments from 1 to 70 m/s.

With these climatological differences in mind, we next examine the location of the occluded cyclones. Here we consider all cyclone instances that are flagged as occluded, including those that belong to the same track. Then we consider the fraction of all cyclone instances in a $5^{o}$x$5^{o}$ region that are identified as occluded. In MERRA-2, the fraction of occluded cyclones tends to be relatively larger in the entrance and middle regions of the storm track in both ocean basins (Figure 2a). There are relatively larger fractions to the west of the dateline than to the east in the Pacific and west of Iceland rather than east of it in the Atlantic. However, the fraction of occluded cyclones in E3 exhibits some clear discrepancies with respect to reanalysis, in both ocean basins (Figure 2b). In the Pacific, the occlusions are more evenly distributed and noticeably more frequent along the Alaskan coast in E3 than in reanalysis. In the Atlantic ocean, they tend to occur more frequently towards the exit region of the storm track than they do in the reanalysis. Cyclones also occlude in the Mediterranean Sea 45% more often in Model E3 than in the reanalysis, though the physical basis for this notable discrepancy is unknown. There is no systematic relation between the discrepancy in preferred occlusion locations and the jet location. Therefore, differences in the large-scale circulation climatology alone do not explain differences in where occlusions are favored in E3.

Examining the occluded portion of the cyclone lifecycles more specifically, we find there are fewer cyclones undergoing occlusion in E3 than in reanalysis (Figure 3a). Figure 3a also reveals a larger variability in the number of occluded cyclones per month in MERRA-2 than E3. However, for those cyclones that do occlude, they tend to do so over a substantially longer period of time in E3 (well over three days; Figure 3b). In other words, E3 occludes less, but has longer lasting occlusions. While it is clear that Model E3 does simulate occluded cyclones, there are some disparities with reanalysis in their preferred location, frequencies and duration. Since these differences cannot be simply explained by differences in the overall model climate, we next explore the structure of the occluded cyclones in E3 to evaluate whether the mechanisms involved in the occlusion process are realistically represented.

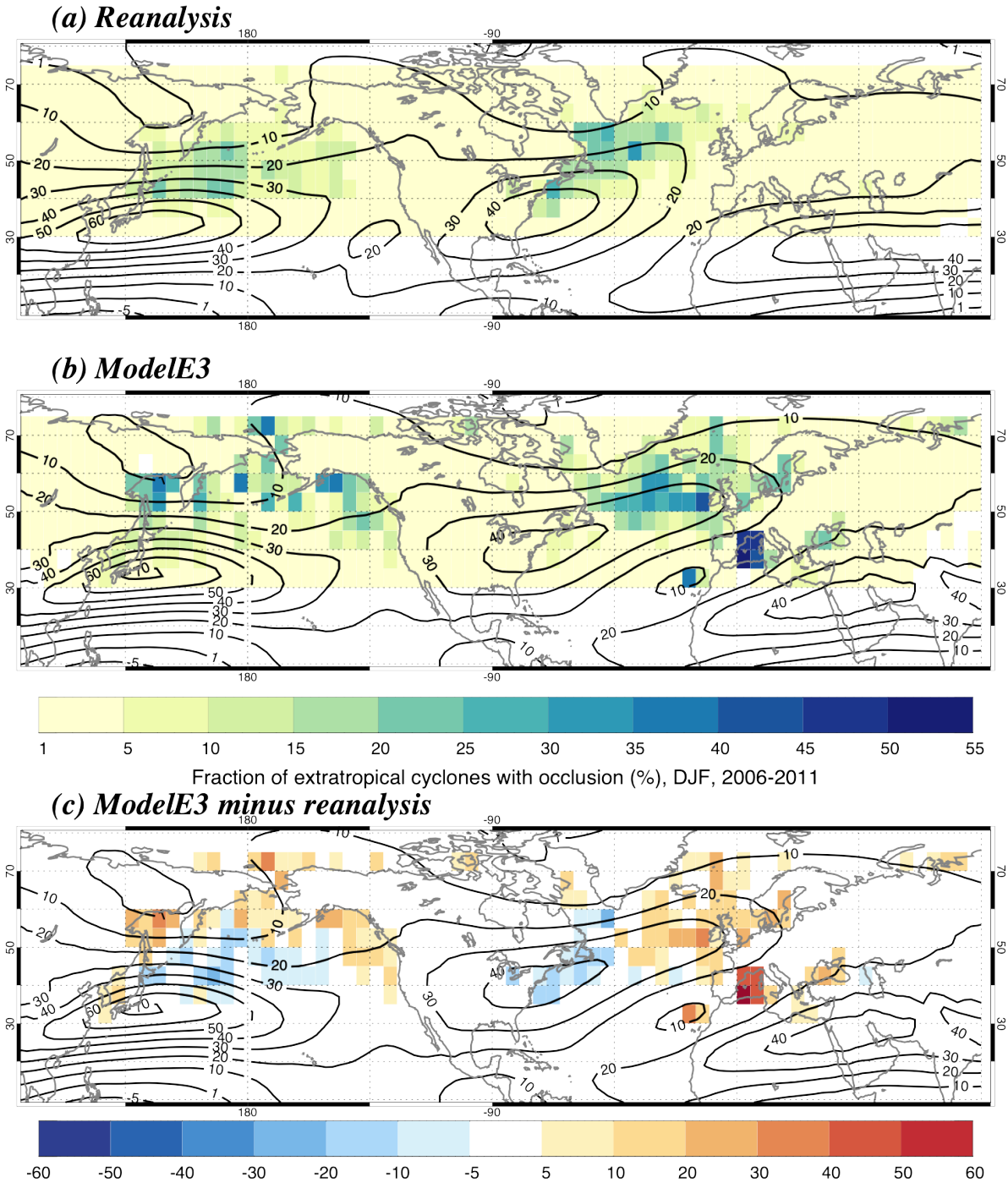


Figure 2: Fraction of all cyclones per 5°x5° cell that are identified as being occluded in (a) the reanalysis and (b) ModelE3 (%, in color, from 1 to 55% in 5% increments). The solid contours indicate the zonal 250hPa wind averaged for times when an occluded cyclone occurs (in m/s, from 1 to 70m/s in 10 m/s increments). (c) shows the corresponding difference between ModelE3 and MERRA-2. Solid contours show the mean 250 hPa zonal wind from Model E3 collected at the time of occlusion.

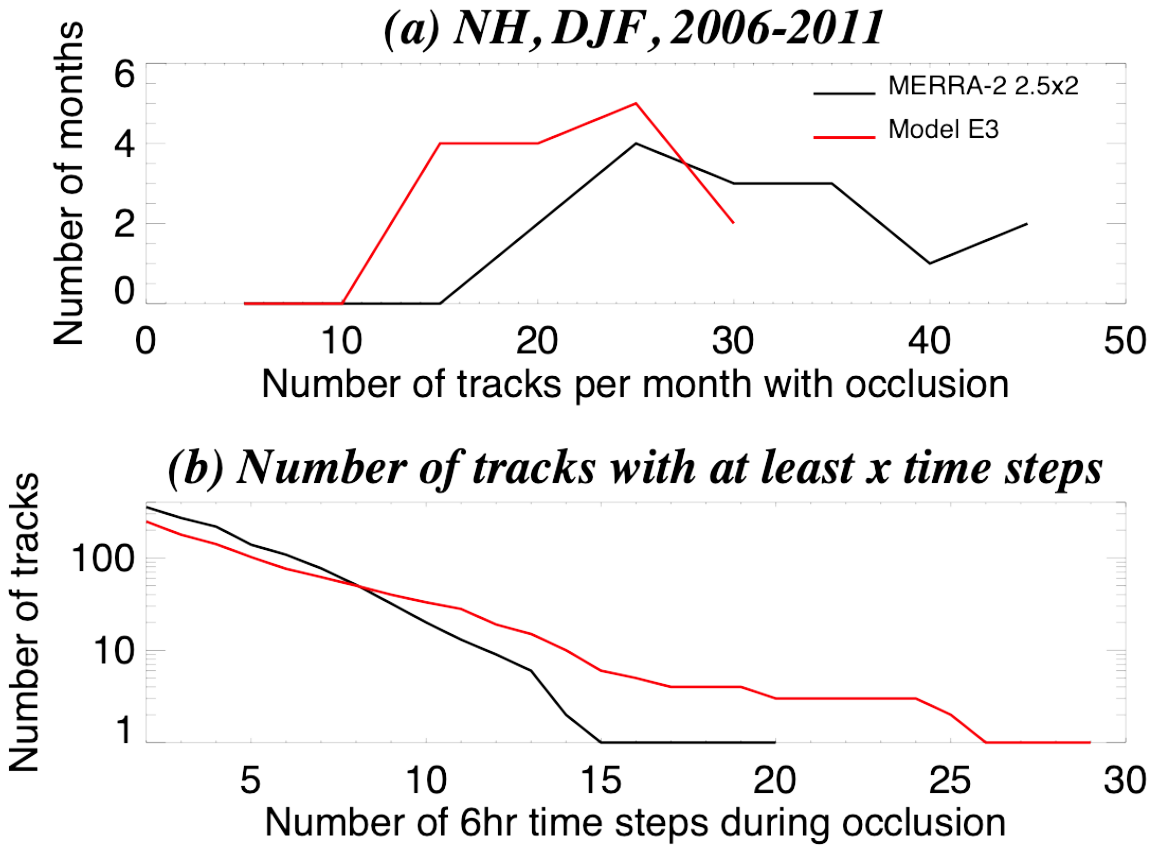


Figure 3: (a) Distribution of the number of tracks that are at some point occluded, per month, for MERRA-2 (black), and Model E3 (red solid) and (b) the total number of tracks with a minimum number of 6-hourly time steps from 2 to 30 in MERRA2 (black) and Model E3 (red solid).

*b. Is the structure of the occluded cyclones in E3 realistic?*

An example of an occluded cyclone in E3 is shown in Fig. 4. Figure 4 provides the $\theta_e$ distribution around the cyclone center at 700 hPa and across the OTR. As is typical of occluded cyclones, the $\theta_e$ field indicates an area to the east of the cyclone center with relatively large values, reflecting the location of the warm and moist air stream that wraps itself cyclonically around the cyclone center (Figure 4a). Joining the inflection points of each contour enables visual establishment of the general location of the OTR. The vertical transect perpendicular to the ridge (A-B line in Figure 4a) reveals a deep thermal structure that coincides with a strong ascent, both typical of the thermal ridge (Figure 4b; c.f. Martin 1998a).

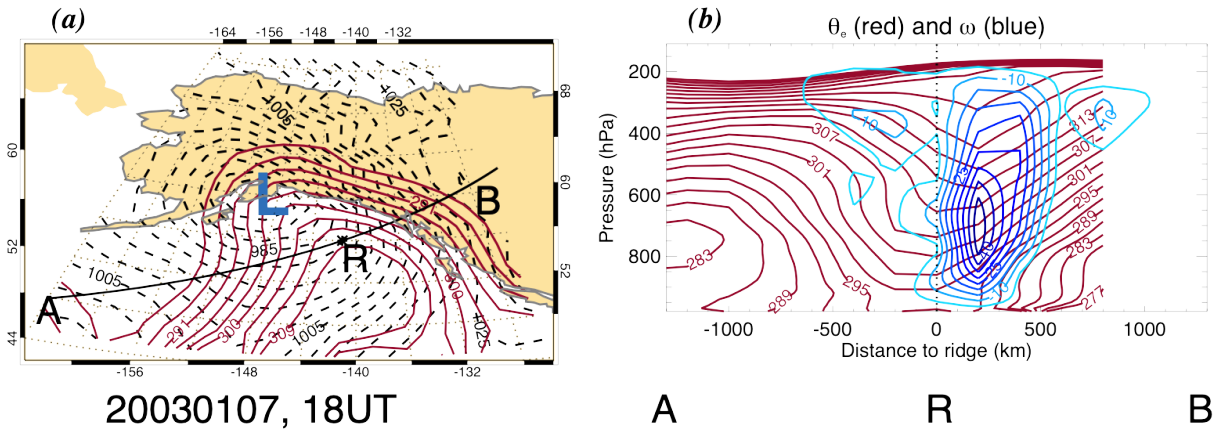


Figure 4: An exemplar of an occluded cyclone simulated in E3 centered at 58.06° N and 149.91° W. (a) Plan view of the sea level pressure field (dashed contour, from 970 hPa in 4hPa increments), and the 700 hPa equivalent potential temperature ($\theta_e$) field (solid red, from 270 K, in 3K increments), with the solid black line representing a transect from A to B perpendicular to the thermal ridge with an intersect at R; (b) the vertical transects from A to B along the perpendicular to the ridge of $\theta_e$ (red contours, from 260 K, in 6K increments) and vertical velocity where ascending (blue contours, from -45 hPa/hr, in 5 hPa/hr increments) as a function of the distance to the ridge intersect at 700 hPa (R) in 200 km increments. The vertical dotted line indicates the location of the ridge at 700 hPa.

To assess whether this example is representative of most occlusions in E3, we build cyclone-centered composites of 700 hPa $\theta_e$ for all DJF NH cyclones in E3 and MERRA-2, as well as composites of the potential vorticity at 200 hPa (Figure 5). These composites are constructed only for the time of maximum intensity during occlusion – that is, when any given occluded cyclone experiences its lowest sea level pressure.

The 700 hPa $\theta_e$ composites show the typical contrast between the warm moist southerly flow and the cold dry northerly flow, with a sharp gradient at the cyclone center and a tongue of relatively higher $\theta_e$ expanding from southeast to northwest just east of the cyclone center, i.e. the thermal ridge. While Model E3 realistically represents the overall thermal structure of the occluded cyclones at their peak intensity, the simulated cyclones have lower $\theta_e$ values at the center and weaker gradients in the vicinity of the thermal ridge (Fig. 5a versus 5b).

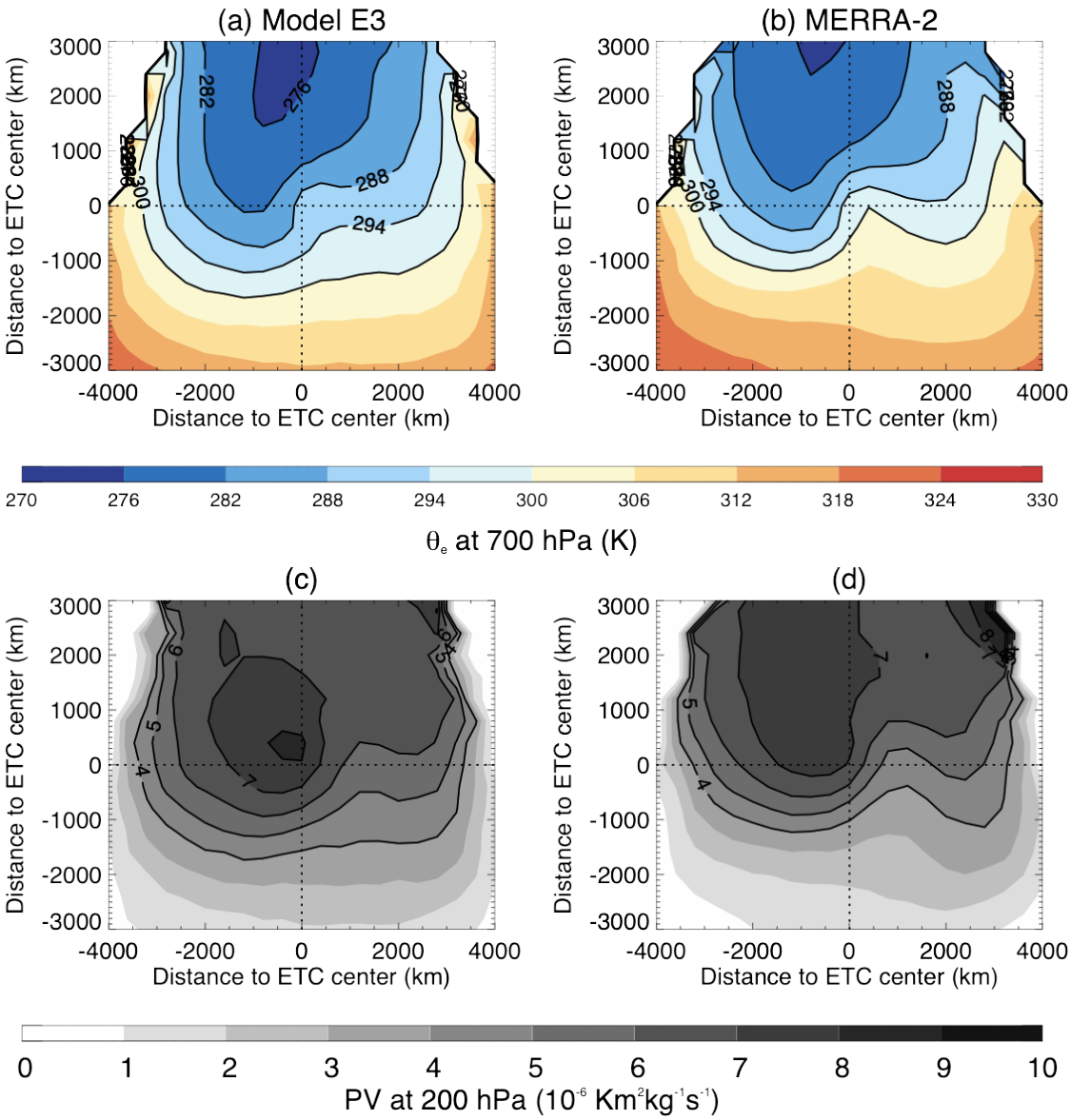


Figure 5: Cyclone-centered composites of equivalent potential temperature at 700 hPa (a, b) and 200 hPa potential vorticity (c,d) for Model E3 (a,c) and MERRA-2 (b, d). The dotted lines intersect at the cyclone center.

The cyclone-centered composites of potential vorticity (PV) reveal a sharp gradient from west to east across the cyclone center, with a maximum in PV just to the northwest of the cyclone center and a tongue of relatively low PV to the east. Strong latent heat release in the thermal ridge causes a decrease in upper-level PV, enhancing the PV gradient and eroding the relatively high PV region to the north of the cyclone center. In individual cyclones, the high PV region close to the cyclone center is connected to a high PV reservoir at higher latitudes through

a narrow filament making the PV distribution resemble the treble clef structure described in Martin (1998a). In the MERRA-2 composite however, the filaments do not align across all cyclones, smearing the treble clef pattern, and a relatively wide area of high PV expanding poleward from just northwest of the cyclone center is found instead (Fig. 5d). While the E3 composite of PV (Fig. 5c) shares similarities with that from MERRA-2, the nearly uniform high PV corridor to higher latitudes in E3 is shorter, presumably because the occluded cyclones in E3 tend to occur at higher latitudes, therefore closer to the high PV reservoir. Additionally, the PV gradient at the cyclone center is weaker, possibly because the latent heating to the east is not as efficient at eroding the PV as suggested by reanalysis. Therefore, while the model is providing a realistic thermal and kinematic structure at both lower- and upper-levels respectively, the composite differences compel further examination of the thermal ridge, with a focus on clouds.

*c. How well are thermal, kinematic and moisture variables represented in the E3 thermal ridge?*

To examine the thermal ridge structure, we construct and analyze vertical transect composites across the thermal ridge as described in Section 2e. Because there are discrepancies in the statistical location of the occluded cyclones in E3 relative to ERA-Interim, there are differences in the mean cyclone-centered $\theta_e$ and PV distributions that tie more to mean state climatology mis-representation and less to cyclone-specific feature differences. To better judge whether the vertical structure of the OTR is well represented in the model, we elect to conduct the ridge comparison between E3 and reanalysis for similar cyclones. To begin, we sort all occluded cyclones according to their max($\theta_e$) at 700 hPa along the ridge. Naud et al. (2023) demonstrated that this quantity was a good metric to quantify the strength and depth of the OTR. In this manner, we facilitate a fairer comparison of the GISS-E3 composite transects of $\theta_e$ and $\omega$ with MERRA-2 for similar thermal ridges. This is achieved by dividing the entire population of thermal ridges into three equal size subsets, using the same max($\theta_e$) thresholds for both the model and reanalysis. A sufficient sample size per max($\theta_e$) category is afforded by the expansion of the analysis to include both hemispheres and all seasons.

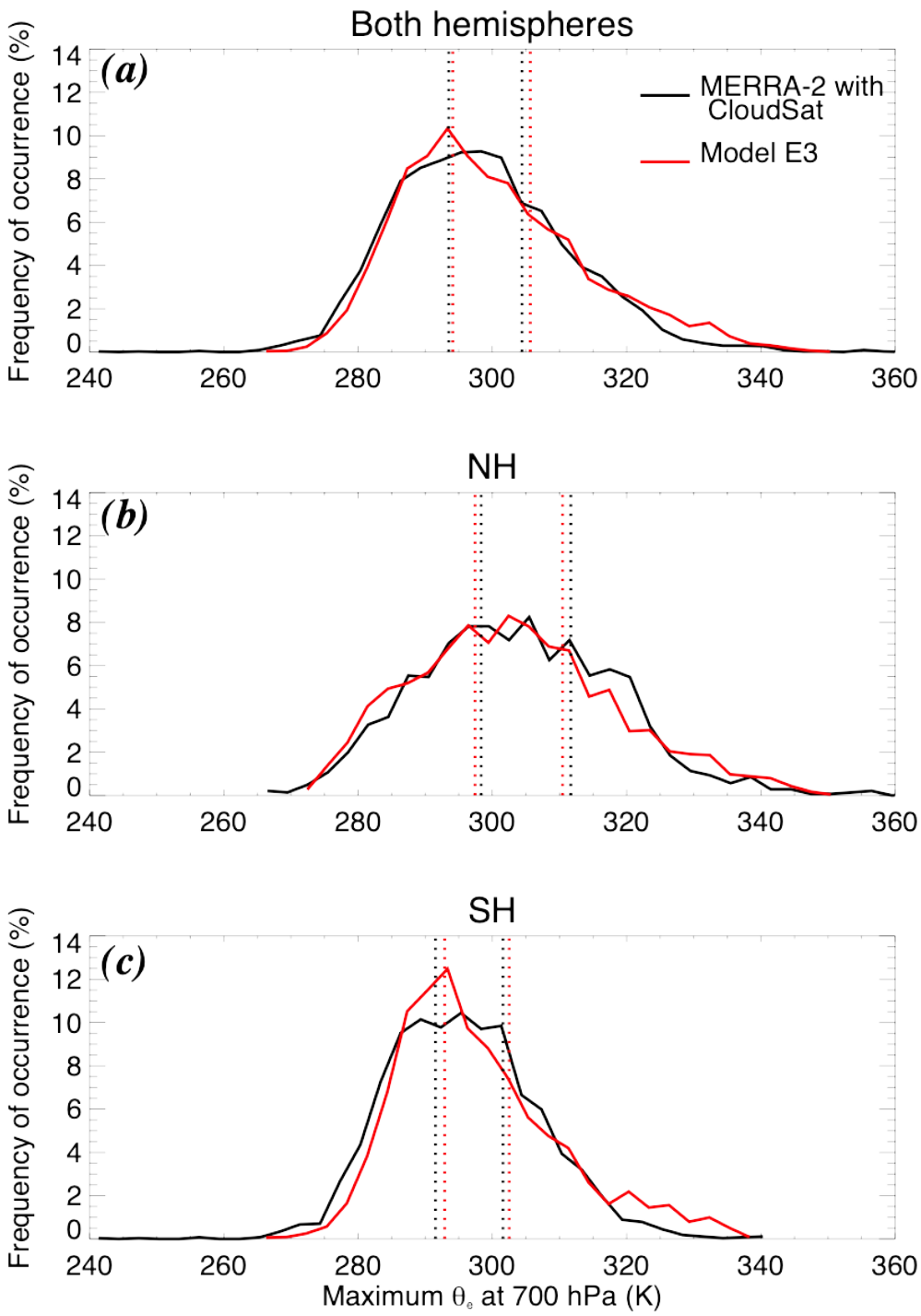


Figure 6: Distribution of $\theta_e$ at 700 hPa in all thermal ridges for all seasons in (a) both hemispheres, (b) in the northern hemisphere only and (c) in the southern hemisphere only, for MERRA-2 (black dashed) and Model E3 (solid red). The dotted lines indicate the $\theta_e$ values that divide the populations into three equal size subsets (red for Model E3, black for MERRA-2).

Next, we use CloudSat-CALIPSO overpasses of thermal ridges to obtain an independent view of hydrometeors across thermal ridges. The narrow swath of the instruments mean that only a subset of all thermal ridges can be observed. To overcome this limitation, we use the full 2006-2017 period with observations to ensure a large enough sample size in our reference dataset. Since the model provides complete information for all thermal ridges, for Model E3, we investigate the same 5-year dataset used in earlier described analyses. With this expanded dataset, we find that both Model E3 and the observational dataset share a very similar distribution of max($\theta_e$) at 700 hPa across all OTRs (Figure 6a), with slightly cooler cases in ModelE3 for the NH (Fig 6b) and warmer ones for the Southern Hemisphere (Fig 6c) relative to MERRA-2. Using the entire population, the three max($\theta_e$) categories are defined as ridges with 1) $\theta_e$ < 294 K, 2) 294 < $\theta_e$ < 304 K, and 3) $\theta_e$ >304 K. These are the categories we anchor against for all the thermal ridge transect comparisons.

Composite transects of $\theta_e$ and vertical velocity ($\omega$) across the thermal ridge (Figure 7) confirm that the single case of Figure 4 is representative of general E3 OTR structure. For each max($\theta_e$) category, E3 thermal structures across the thermal ridge are very similar to their MERRA-2 counterparts, with E3 simulating comparable variation in $\theta_e$ transects from one max($\theta_e$) category to the next. The "warmest" category exhibits the closest match to a canonical structure of a thermal ridge as discussed in Naud et al. (2023) and it is realistically represented by E3 (Fig. 7c versus 7f).

While E3 is also comparable to MERRA-2 with respect to $\omega$, with a maximum slightly poleward of the thermal ridge and a clear vertical expansion and increased tilt with increasing max($\theta_e$), the maximum in ascent strength is lower in the model, with differences in maximum at the ridge of at least 2 hPa/hr (for the closest, medium max($\theta_e$) category, Fig. 7g vs. 7j). This may be due to the coarser spatial resolution of E3 compared to MERRA-2. However, the reanalysis indicates that vertical velocities are the strongest for the warmest max($\theta_e$) category, while the model produces the greatest ascent strength for the medium max($\theta_e$) category. To test whether this discrepancy might have consequences for clouds and precipitation in the thermal ridge, which in turn would affect latent heat release as well as its impact on occlusion persistence and overall evolution, we next examine composite transects of cloud fraction.

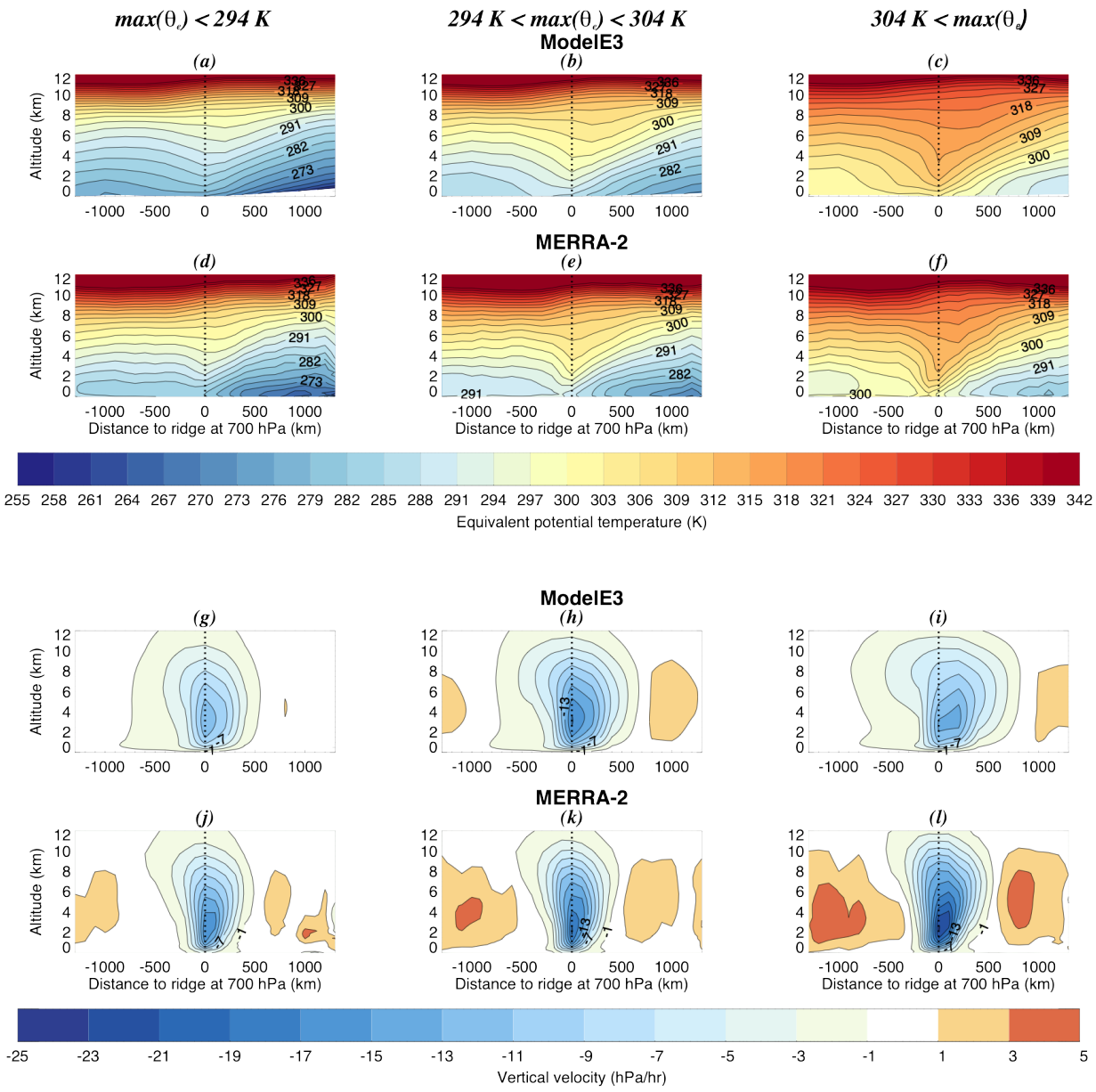


Figure 7: Composite transects across the thermal ridge of (a-f) $\theta_e$ and (g-l) vertical velocity for ModelE3 (a-c, g-i) and MERRA-2 (d-f, j-l) for three categories from (a,d,g,j) $\theta_e < 294K$, (b,e,h,k) $294 < \theta_e < 304$ K and (c,f,i,l) $\theta_e > 304$ K. In each subplot, the vertical dashed line marks the location of the thermal ridge at 700 hPa, the x-axis is the distance to the ridge (in km), and the y-axis the altitude (in km).

Using Model E3 profiles of cloud fraction, we build composite transects following the same method used for $\theta_e$ and $\omega$ transects. The model cloud fraction is computed as the sum of convective and stratiform cloud fraction (including precipitation fraction) as viewed by the

model radiation scheme. As discussed previously, the observed profiles are not evenly distributed in space, and instead are provided along the satellites orbit (c.f. Section 2e; Naud et al., 2024). Therefore we only sample some portion of the thermal ridge area for each case. In Naud et al. (2024), it is shown that by compositing multiple cases the impact of this sparse coverage can be alleviated. The observation-based composite transects are the sum of all observed profiles of the hydrometeor mask (with 1s where GEOPROF-LIDAR indicates a cloud layer, 0s otherwise) normalized by the total number of profiles. The result is a frequency of hydrometeor occurrence across the thermal ridge. Some differences between Model E3 and observations can arise due to precipitation contamination in the observations attenuating radar signals to such an extent that hydrometeors at lower altitudes are not observable.

Figure 8 shows the composite transects of E3 cloud fraction per max($\theta_e$) category and the corresponding transects of hydrometeor frequency of occurrence obtained from CloudSat-CALIPSO. Regarding simulated versus observed hydrometeor transects for each max($\theta_e$) category independently, E3 exhibits larger cloud fractions above 8 km than observed along with a tendency to expand further poleward at those altitudes as well. This is true for all three max($\theta_e$) categories. At those altitudes, the CALIPSO lidar is less often attenuated and the observations are quite accurate as a result. Therefore, it is probable that the E3 overestimation of cloud fraction (by at least 5-10%) is a robust result at those higher altitudes. This overestimate may arise from 1) tuning parameter settings, for example the critical relative humidity thresholds, which aim to satisfy zonal and global constraints, but are not regime-dependent (i.e., cyclone specific); or, when embedded convection occurs, 2) a too-weak sink term of stratiform anvil cloud area (possibly due to too little IWC seeding stratiform rainfall; Elsaesser et al., 2022) or 3) overactive detrainment of slowly-sedimenting small-ice particles from any embedded convective clouds (e.g., Elsaesser et al. 2017a). Consistent with the latter possible cause, the Geophysical Fluid Dynamics Laboratory (GFDL) model was found to have a similar overestimate in cloud fraction above 10 km in the cold frontal region of extratropical cyclones (Naud et al., 2019): this was attributed to a relatively weak ice crystal fall speed, implying that ice is suspended for longer timescales than are realistic.

In contrast to the higher altitude results, CloudSat-CALIPSO displays a maximum in hydrometeor frequency at low altitudes (below 5 km), where only the radar can sense hydrometeors, and where precipitating hydrometeors tend to be more frequent. The lower cloud fractions in Model E3 at these altitudes may be consistent with a weak ice fall speed as well or reflective of model tuning choices once again (see discussion above). This can indicate a bifurcated behavior, where ice either remains suspended and slowly evaporates at high altitudes, or it falls out as precipitation, but never sediments at the correct moderate speeds to facilitate vertical expansion of the cloud depth.

Despite these differences in overall distribution, the model does reproduce the contrasts between max($\theta_e$) categories similarly to observations: cloud tops expand upward and poleward from low to high $\theta_e$ categories. As previously reported in Naud et al. (2024) for the observations, the maximum in cloud fraction in the largest $\theta_e$ category is less than that of the middle $\theta_e$ category. However, the drop in maximum cloud fraction from medium to high max($\theta_e$) ridges is more dramatic in E3 than observed (in fact it is barely noticeable in the observed transects), which is possibly exacerbated by the concurrent drop in ascent strength that only E3 produces. As a result, latent heat release in the E3 thermal ridge in those high max($\theta_e$) cases is almost certainly too weak. In contrast, increased cloud at high altitudes in low and medium max($\theta_e$) ridges may imply stronger latent heat release, potentially assisting in maintaining the ridge over relatively long periods of time, thus potentially explaining the more frequent long-lived occlusions in E3 for cyclones that are overall occurring at higher latitudes than observed.

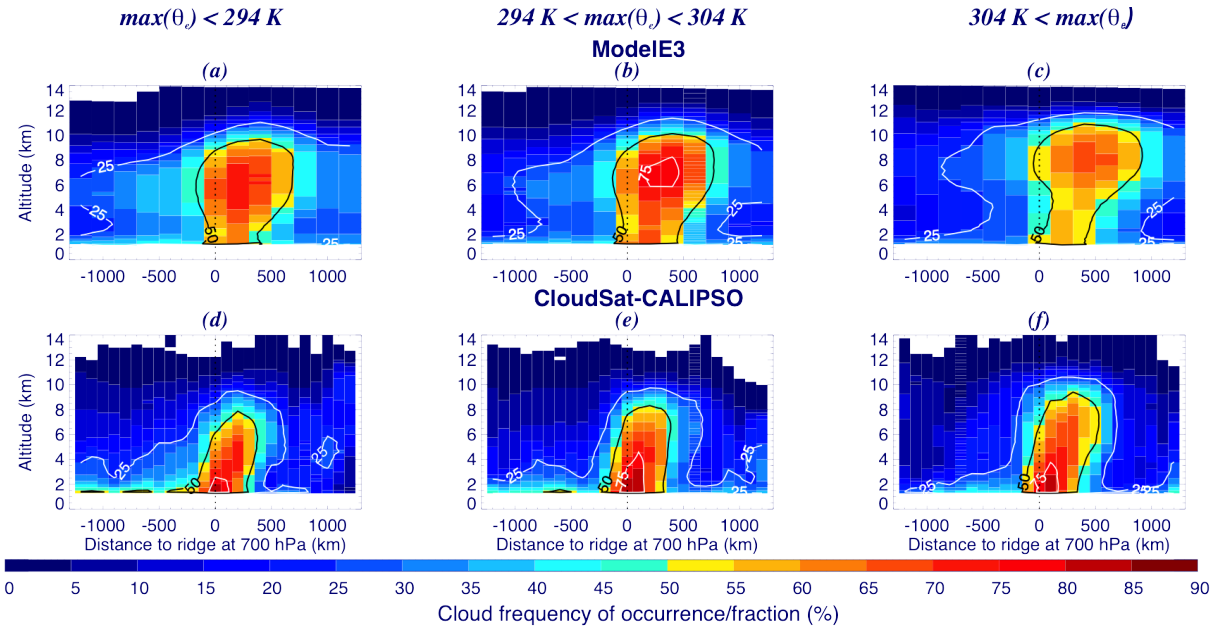


Figure 8: Composite transect of model E3 cloud fraction (a-c) across the thermal ridge for three $\theta_e$ categories, and corresponding transects of CloudSat-CALIPSO cloud frequency of occurrence (d-f). (a,d) include thermal ridges with $\theta_e$ at 700 hPa < 294K, (b, e) 294 < $\theta_e$ < 304 K, and (c,f) 304 K < $\theta_e$. In each panel, the vertical dotted line indicates the location of the thermal ridge, and the solid black and white contours the 25, 50 and 75% fraction/frequency levels.

Because cloud fraction only describes where and when clouds form, it does not relay information regarding how tenuous those clouds might be. Therefore, we analyze a different diagnostic of the cloud state: composite transects of ice water content. These data are provided by the 2C-ICE product, and we utilize the same compositing strategy as that used for hydrometeor frequency, i.e. the vertical profiles of hydrometeor presence/absence are replaced with profiles of ice water content. To separate out the impact of changing hydrometeor frequency from one max($\theta_e$) category to the next, ice water content is only averaged where ice is present, i.e. IWC > 0 $gm^{-3}$. Because 2C-ICE relies on a combination of information from both lidar and radar, greater uncertainties are expected in cloud areas where only one of the two instruments can detect hydrometeors. The lidar signal is superior at detecting small particles often found near cloud top that the radar cannot detect, and inversely, the lidar signal gets attenuated in thick clouds leaving radar reflectivities solely available at lower altitudes (Deng et al., 2010). Profiles of E3 IWC are composited with the same method used for the other variables, as described, but after a re-set of IWC to zero if below the thresholds discussed in

Section 2b. The model provides ice mass for both stratiform and convective cloud, including precipitating components. Here we use the sum of all four components.

For each max($\theta_e$) category, Model E3 simulates lower values of IWC than reported from 2C-ICE (Figure 9). However, the overall distribution of IWC with altitude exhibits a more realistic pattern than the cloud fraction, with larger mass at lower rather than higher altitudes, as would be expected in environments where available moisture is maximized at lower levels. Below the 50% model cloud occurrence level (c.f. Fig. 8a, b, c), while the model reproduces the variations in IWC across the ridge, with a maximum at and poleward of the ridge, the overall magnitude is less than observed. This implies that E3 produces clouds too often but with less ice than observed, suggesting a "too many, too tenuous" high-level cloud bias in contrast to what has often been reported in most ESM analyses at lower altitudes: the "too few, too bright" cloud problem (e.g. Nam et al., 2012 and references therein; Konsta et al., 2022). At lower altitudes with a temperature range where mixed phases occur, part of the discrepancy might be caused by supercooled liquid contamination in the observations, which would impact the lower altitudes more than the higher altitudes because lidar attenuation would occur, leaving only radar reflectivities as input to the 2C-ICE algorithm. This would cause an overestimate of IWC at altitudes and temperatures where liquid can persist. Additionally, biases could be reflective of differences in temperature thresholds for assumed ice – liquid partitioning in CloudSat-CALIPSO versus the GISS model: for the latter, liquid extends to colder temperatures, thus lower ice cloud fractions.

For occlusions in general, simulated and observed transects reveal a clear increase in IWC from low to medium to high max($\theta_e$) thermal ridges. Therefore, while the "warmest" thermal ridges may have less frequent clouds than their slightly "cooler" counterparts, they do contain more ice, which is consistent with larger precipitation rates as reported in Naud et al. (2024). Remarkably, the model represents these contrasts well, lending confidence that it reproduces the moist processes in these occluded systems in a fairly realistic way. However, the lower IWC overall impacts the model's representation of latent heating, which could contribute to the weaker PV erosion aloft, and possibly the lower overall occurrence of occlusions.

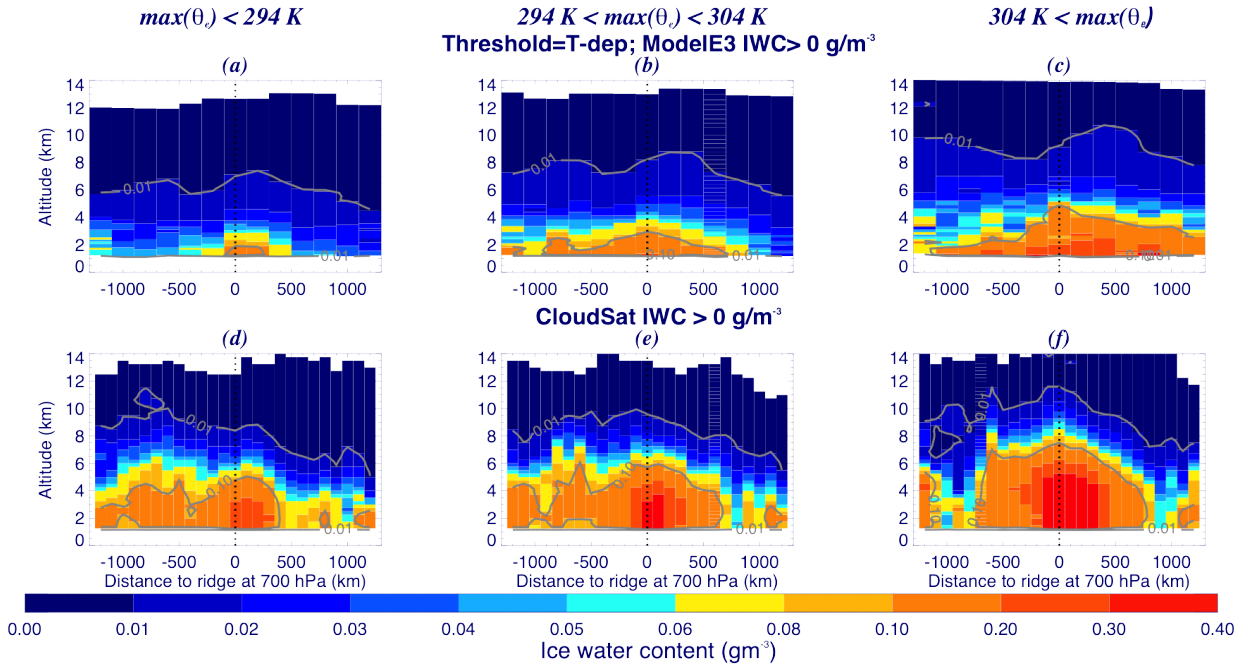


Figure 9: Composite transects of conditional IWC (i.e, average over all scenes for IWC > 0) from (a-c) Model E3, and (d-f) CloudSat-CALIPSO (2C-ICE) for the three thermal ridge categories: (a, d) max($\theta_e$) < 294 K, (b, e) 294<max($\theta_e$) < 304 and (c, f) 304 K < max($\theta_e$). In each panel the vertical dashed line represents the location of the thermal ridge at 700 hPa. The light grey contours show the 0.01 and 0.1 gm$^{-3}$ IWC levels.

## 4. Discussion

Analyses thus far have verified that 1) an ESM can produce occluded cyclones, 2) it does so with realistic thermal and kinematic structures, but 3) with some possible biases in the representation of ascent strength, cloud coverage and ice mass. While these issues may connect to the number of occluded cyclones, their location and their longevity, they do not affect the ability of the model to represent a realistic sensitivity of clouds in the thermal ridge to the thermodynamic characteristics of the thermal ridge. Here we address two subsequent questions: how unique is E3 in its representation of occlusions, and why should E3 or any ESM represent occlusions realistically?

### *a. How unique is Model E3?*

One way to test whether E3 is unique is to conduct a similar analysis of its predecessor, GISS-E2.1 (Kelley et al., 2020). The advantage of employing E2.1 for such a test is that the differences between the two models are well documented and most are related to the

treatment of moist processes (e.g. Cesana et al. 2019; Russotto et al., 2022). Section 2a lists the most salient improvements implemented between E2.1 and E3. As for E3, we apply the same occlusion finding algorithms to a free-running integration of E2.1 over years 2006-2011 using the same prescribed monthly mean temperatures as was used for E3. First, the cyclone tracker described in Section 2c is applied, followed by implementation of the occlusion identification method (Section 2d). Discussing all analyses performed thus far would be untenable, so only the most salient results are illustrated here.

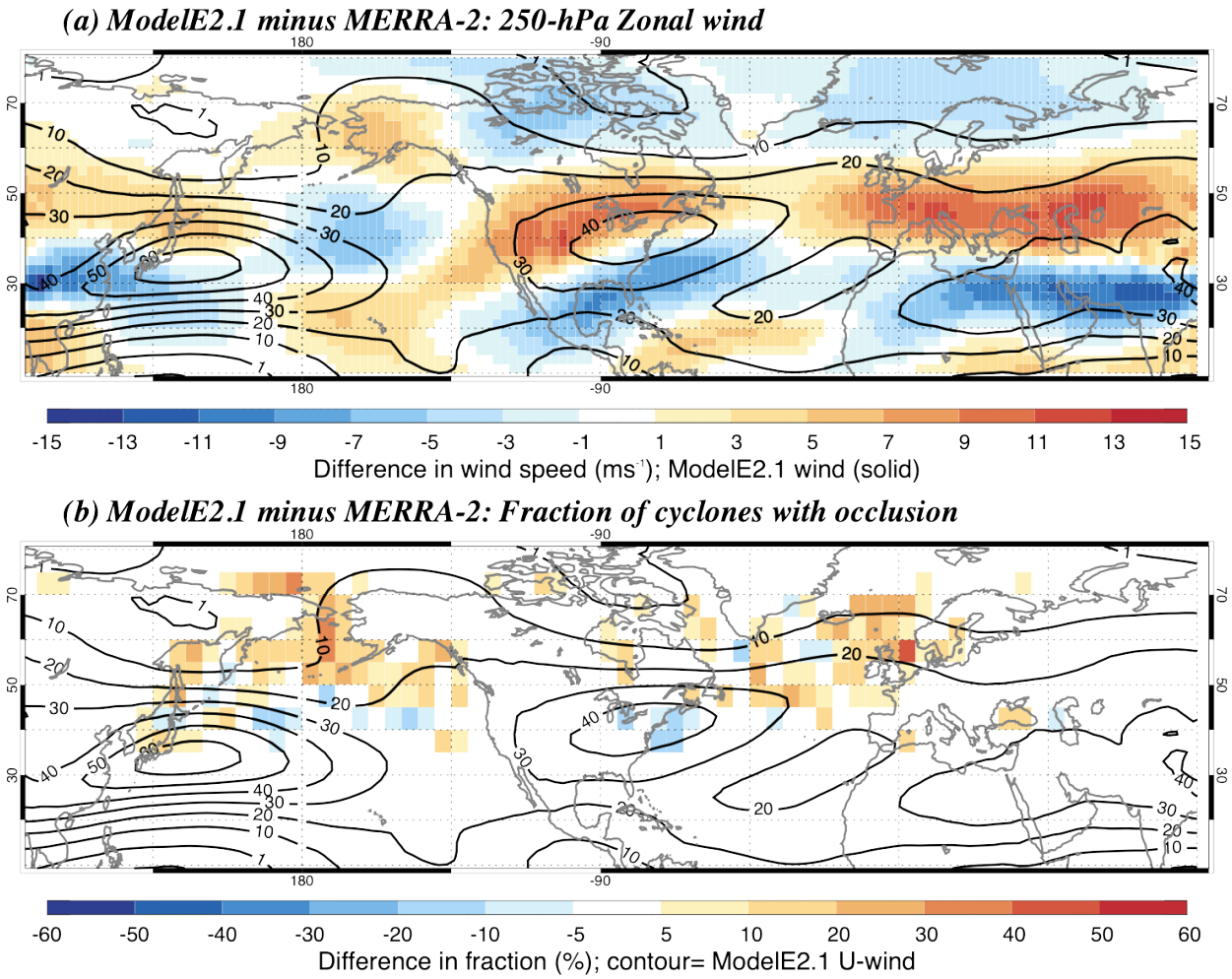


Figure 10: Maps of the difference between Model E2.1 and MERRA-2 in (a) 250 hPa zonal wind (in color), with the Model E2.1 jet as solid contours (from 10 to 70 m/s in 10 m/s increments) and (b) the fraction of cyclones that are occluded (in color), with the Model E2.1 jet as solid contours (from 10 to 70 m/s in 10 m/s increments).

We find that E2.1 can also produce occlusions. The upper-level jets in E2.1 are more zonally oriented than those in E3 or MERRA-2 and the north Atlantic jet is shifted poleward (Fig. 10a). However, there is no clear link between this jet discrepancy and the difference in the preferred location of occlusions between E2.1 and MERRA-2 (Fig. 10b vs. 10a). As was found with E3, E2.1 tends to overestimate the fraction of cyclones that occlude along the Alaskan coast and from Iceland to Scandanavia, while underestimating their occurrence near the entrance region of the north Atlantic or the southern edge of the Pacific storm tracks (Fig. 10b). While the thermal and kinetic structures of the occluded cyclones in E2.1 resemble the reanalysis, E2.1 exhibits similar weaknesses in the PV structure as was found for E3 (not shown), i.e. a weaker erosion of high PV in the area where latent heat release is maximum in the thermal ridge. Focusing next on the thermal ridge and applying the same subsetting based on the ridge max($\theta_e$) metric, E2.1 also reproduces a realistic thermal and kinematic structure of the ridge (Figs. 11a-f). However, not only is the vertical velocity weaker than in the reanalysis, it also appears weaker than that depicted in E3 (about 2hPa/hr difference in maximum for the middle max($\theta_e$) category, Fig. 11e vs. Fig. 7g). As a result, cloud fraction across the OTR is lower in E2.1 than E3, and the drop between ridges in the middle and high max($\theta_e$) categories is even more dramatic, with very infrequent clouds below 5 km. Of note as well is a weaker tilt of the cloud distribution across the thermal ridge when compared to E3 and observations. Thus, this analysis reveals that E3's representation of occlusions is not unique, and to that end, other somewhat less advanced models may also faithfully depict elements of the canonical occluded structure and its cloud and precipitation characteristics. But the analysis also demonstrates the importance of improvements in the representation of clouds and precipitation for a more accurate representation of the thermal ridge. Next, we discuss why representing the thermal ridge adequately is important for an ESM.

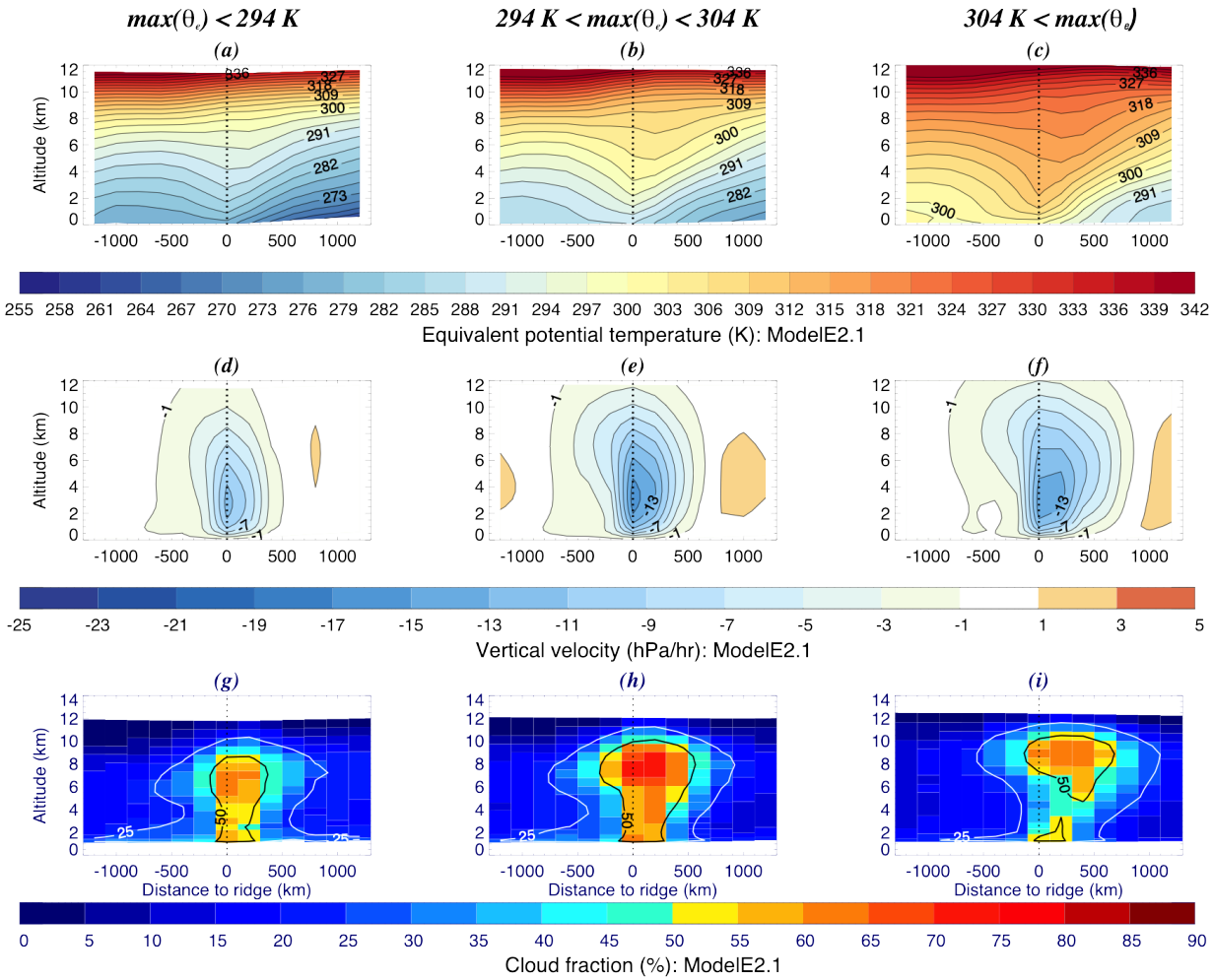


Figure 11: Composite transects across the thermal ridge of E2.1 (a-c) equivalent potential temperature, (d-f) vertical velocity, and (g-i) cloud fraction for (a, d, g) max($\theta_e$) < 294 K, (b, e, h) 294<max($\theta_e$) < 304 and (c, f, i) 304 K < max($\theta_e$). In each panel the vertical dashed line represents the location of the thermal ridge at 700 hPa.

*b. Why should ESMs represent realistic occlusions?*

Now that we have established that E3 is producing realistic occlusions, we attempt to demonstrate why this is important in a climatological context and why further improvements in the simulation of clouds and precipitation in the model are necessary. To begin, we explore the mean precipitation in E3 cyclones that have reached their peak intensity. These simulated cyclones mirror the real-world storms that are responsible for the most extreme precipitation, flooding events, and extreme windstorms. Here we further separate these cyclones at peak intensity into those that, at some point in time, occlude, and those that never do (according to the identification method outlined in Section 2d). One caveat is that the occlusion identification

method is conservative. It is designed to excel at identifying cyclones that are occluded, but tends to reject ambiguous cases. Therefore, the cyclones at peak intensity that are categorized as “unoccluded” might include some occluded cyclones.

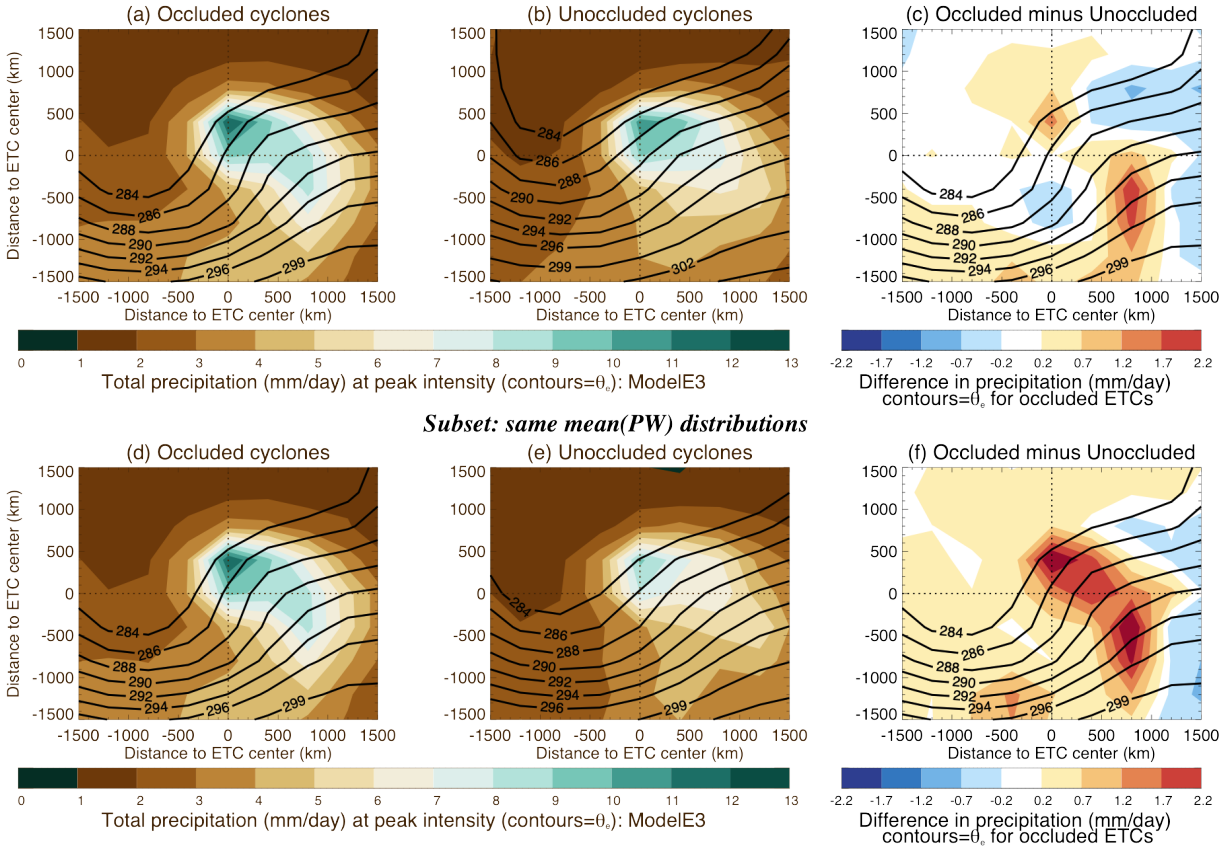


Figure 12: Cyclone-centered composites of E3 surface precipitation rates (in color) for (a) occluded cyclones and (b) unoccluded cyclones at peak intensity, with solid contour showing their associated composite of equivalent potential temperature (in 2K intervals from 284 K) . (c) Difference in precipitation between occluded and unoccluded cyclones, with solid contours showing the composite of equivalent potential temperature of occluded cyclones. (d, e, f) show similar composites to (a, b, c) but for a subset of cyclones at peak intensity for which both occluded and unoccluded subsets share the same distribution of mean(PW) across cyclones. The dotted lines intersect at the cyclone’s center.

Cyclone-centered composites of surface precipitation are constructed for each subset of cyclones (Fig. 12a-b). These composites reveal that in E3, cyclones that do occlude produce more precipitation than those that do not, with differences up to 1.5-2 mm/day at the locations where cyclones in general produce most of the precipitation (Figure 12c), i.e., northwest of the

cyclone center, in the region that is the peak of the warm sector for occluded cyclones and into the pre-cold frontal (warm sector) region. However, upon inspection of the properties of the two sets of cyclones, it appears that the unoccluded cyclones include a greater fraction of systems with large mean precipitable water (PW) in their environment (22% have PW > 13 mm, compared to 6% of occluded cyclones). PW and precipitation are highly correlated in cyclones (e.g. Field and Wood, 2007; Booth et al. 2018; Sinclair and Catto, 2023), thus we sort the two sets of cyclones to force the mean cyclone-wide PW distribution across all cyclones in each subset to match. This is achieved by randomly removing cyclones from each set until both sets include the same number of cyclones with a given mean PW within 1 mm. For these two sets of occluded and unoccluded cyclones with matching PW distributions, the difference in precipitation is much larger, as might be expected, but not yet documented (Figure 12d-f). This suggests that E3 occluded cyclones are more efficient at processing PW into precipitation. This further demonstrates that occluded cyclones play an important role in the production of precipitation and its extremes, and that ESMs must faithfully reproduce this stage in the cyclone life cycle to accurately represent precipitation totals, their future changes and their extremes.

## 5. Conclusions

Using a novel method for identifying extratropical cyclones that undergo an occlusion, the most recent version of the GISS Earth System Model (E3) is tested for its ability to represent occlusions, their structure and their associated cloud field. Though Model E3 can simulate the occlusion process, compared to the MERRA-2 reanalysis it tends to 1) underestimate the number of tracks with occlusion, 2) place the occlusions too far poleward and 3) simulate long-duration occlusions too often. However, the thermal and kinematic structure of the occluded cyclones and attendant thermal ridges are reasonably well represented in the model. An analysis of CloudSat-CALIPSO GEOPROF-LIDAR hydrometeor retrievals against E3 reveals that the E3 cloud distribution across thermal ridges, while displaying a reasonable sensitivity to the thermal ridge characteristics, tends to be top-heavy, i.e. the model has a tendency to produce high clouds too frequently and over a wider area than suggested by satellite data. This is possibly related to the threshold in relative humidity used for governing cloud formation in E3,

too weak precipitation processes associated with too little IWC and small particle sizes in subtropical to higher latitude stratiform cloud (which serves as a sink for cloud area), and/or ice crystal fall speed. When ice water content transects are compared to CloudSat-CALIPSO 2C-ICE retrievals, a more realistic vertical distribution of condensate amounts is produced by E3, albeit with less ice than reported by 2C-ICE. This issue of "too many, too tenuous" high-level clouds is not unique to E3 (e.g. Naud et al., 2019), and should inform needed model developments as modelling centers prepare for CMIP7. Nevertheless, the model reproduces the sensitivity to thermal ridge characteristics reasonably well. An examination of an earlier GISS CMIP6 model (E2.1) reveals that this previous version also represents occlusions adequately, but with weaker ascent strength and less cloud than E3. Differences are a bulk measure of the impact of the various upgrades (convection, stratiform, boundary layer, tuning) to the representation of moist processes in E3, along with an increase in vertical resolution.

Extratropical cyclones should be well-represented in ESMs because of their important role in the meridional transport of heat and moisture, but also for the production of precipitation, and its extremes. Here, using E3 cyclone-centered precipitation, we demonstrate that the life cycle of these systems also requires adequate representation because occluded cyclones in the model are a lot more efficient at converting moisture into precipitation compared to cyclones that never occlude. The next step will be to use E3 to explore occluded cyclones in a warmer climate toward quantifying how an increased global temperature might influence the occlusion process and associated precipitation. As models' resolution and sophistication increase, the impact of microphysical processes on occlusions and how they might be represented in models will also benefit from increased scrutiny. Such efforts will be aided by adding more vertically-resolved observations and improved IWC and particle size measurements in general, such as those jointly retrieved from the radar and microwave radiometer aboard GPM, retrievals from in-development ice-sensing satellite missions (e.g., the Polarized Submillimeter Ice-cloud Radiometer – PolSIR - sampling the most equatorward cyclone-associated ice clouds), and in the near future, radar and lidar data from the European Space Agency Earth Cloud Aerosol and Radiation Explorer mission (EarthCARE; Illingworth et al., 2015).

*Acknowledgments.*

The work was funded by the NASA CloudSat-CALIPSO science team recompete program, grant number 80NSSC20K0085. CMN and DJP received additional funding from the NASA Modeling, Analysis and Prediction program, grant number 80NSSC21K1728. GSE acknowledges additional related support from the NASA Modeling, Analysis and Prediction Program and APAM-GISS Cooperative Agreement 80NSSC18M0133, NASA Precipitation Measurement Missions grant 80NSSC22K0609, and the NASA PolSIR project (80LARC24CA001). A portion of this research was conducted at the Jet Propulsion Laboratory, California Institute of Technology, under a contract with the National Aeronautics and Space Administration (NASA) 80NM0018D0004. Computing resources for the work were provided by the NASA High-End Computing (HEC) program through the NASA Center for Climate Simulation (NCCS) at the Goddard Space Flight Center. The authors thank Min Deng and Matthew Lebsock for detailed information on the strengths and weaknesses of CloudSat and CALIPSO measurements and products.

*Data Availability Statement.*

The database of occluded cyclones and the database of cyclones with cold and warm front identifications are described and accessible here: https://data.giss.nasa.gov/storms/obs-etc/.
CloudSat-CALIPSO 2B-GEOPROF-LIDAR and 2C-ICE data files are documented and available here: https://www.cloudsat.cira.colostate.edu/.
MERRA2 profiles of temperature, specific humidity, wind and vertical velocity information are available in these files:
Global Modeling and Assimilation Office (GMAO) (2015), MERRA-2 inst3_3d_asm_Np: 3d,3-Hourly,Instantaneous,Pressure-Level,Assimilation,Assimilated Meteorological Fields V5.12.4, Greenbelt, MD, USA, Goddard Earth Sciences Data and Information Services Center (GES DISC), Accessed: 2020-01, 10.5067/QBZ6MG944HW0
Global Modeling and Assimilation Office (GMAO) (2015), MERRA-2 inst6_3d_ana_Np: 3d,6-Hourly,Instantaneous,Pressure-Level,Analysis,Analyzed Meteorological Fields V5.12.4, Greenbelt, MD, USA, Goddard Earth Sciences Data and Information Services Center (GES DISC), Accessed: 2020-01, 10.5067/A7S6XP56VZWS.

REFERENCES

Bauer, M. and A. D. Del Genio, 2006: Composite analysis of winter cyclones in a GCM: Influence on climatological humidity. *J. Climate,* 19, 1652-1672.

Bauer M., G. Tselioudis and, W. B. Rossow, 2016: A new climatology for investigating storm influences in and on the extratropics. *J. Appl. Meteorol. Clim.* 55 1287–303

Bengtsson L., K. I. Hodges, and N. Keenlyside, 2009: Will extratropical storms intensify in a warmer climate? J. Climate, 22, 2276-2301, doi:10.1175/2008JCLI2678.1.

Binder, H., Boettcher, M., Joos, H. and Wernli, H. (2016) The role of warm conveyor belts for the intensification of extratropical cyclones in Northern Hemisphere winter. Journal of the Atmospheric Sciences, 73, 3997–4020

Bjerknes, J., and H. Solberg, 1922: Life cycle of cyclones and the polar front theory of atmospheric circulation*. Geofys. Publ*., 3 (**1**), 1–18.

Booth J. F., C. M. Naud, J. Willison, 2018: Evaluation of Extratropical Cyclone Precipitation in the North Atlantic Basin: An analysis of ERA-Interim, WRF, and two CMIP5 models. *J. Climate*, 31:6, 2345-2360.

Bretherton, C. S., and S. Park, 2009: A new moist turbulence parameterization in the community Atmosphere Model. *J. Climate*, **22**, 3422-3448.

Catto, J. L., C. Jakob, G. Berry and N. Nicholls 2012: Relating global precipitation to atmospheric fronts. Geophys. Res. Lett., 39, L10805, doi: 10.1029/2012GL051736.

Catto, J. L., C. Jakob, and N. Nicholls, 2015: Can the CMIP5 models represent winter frontal precipitation? *Geophys. Res. Lett.*, **42**, 8596-8604, doi:10.1002/GL2015GL066015.

Cesana, G., A.D. Del Genio, A.S. Ackerman, M. Kelley, G. Elsaesser, A.M. Fridlind, Y. Cheng, and M.-S. Yao, 2019: Evaluating models' response of tropical low clouds to SST forcings using CALIPSO observations. *Atmos. Chem. Phys.*, **19**, 2813-2832, doi:10.5194/acp-19-2813-2019.

Cesana, G. V., A. S. Ackerman, A. M. Fridlind, I. Silber, and M. Kelley, 2021: Snow reconciles observed and simulated phase partitioning and increases cloud feedback. *Geophysical Research Letters*, **48**, e2021GL094876. https://doi.org/10.1029/2021GL094876.

Cheng, Y., V.M. Canuto, A.M. Howard, A.S. Ackerman, M. Kelley, A.M. Fridlind, G.A. Schmidt, M.S. Yao, A. Del Genio, and G.S. Elsaesser, 2020: A second-order closure turbulence model:

New heat flux equations and no critical Richardson number. *J. Atmos. Sci.*, **77**, no. 8, 2743-2759, doi:10.1175/JAS-D-19-0240.1.

Crocker, A., W. L. Godson, and C. M. Penner, 1947: Frontal contour charts. *J. Atmos. Sci*., 4 **(3),** 95–99.

Dee D. P., and co-authors., 2011: The ERA-Interim reanalysis: configuration and performance of the data assimilation systems. *Quart. J. R. Meteorol. Soc.*, 137, 553-597.

Del Genio, A.D., J. Wu, A.B. Wolf, Y.H. Chen, M.-S. Yao, and D. Kim, 2015: Constraints on cumulus parameterization from simulations of observed MJO events. *J. Climate*, **28**, no. 16, 6419-6442, doi:10.1175/JCLI-D-14-00832.1.

Deng, M., G. G. Mace, Z. Wang, and H. Okamoto, 2010: Tropical Composition, Cloud and Climate Coupling Experiment validation for cirrus cloud profiling retrieval using CloudSat radar and CALIPSO lidar, J. Geophys. Res., 115, D00J15, doi:10.1029/2009JD013104 (6)

Deng M, Gerald G. Mace, Zhien Wang, and R. Paul Lawson, 2013: Evaluation of Several A-Train Ice Cloud Retrieval Products with In Situ Measurements Collected during the SPARTICUS Campaign. J. Appl. Meteor. Climatol., 52, 1014–1030.

Elsaesser, G.S., A.D. Del Genio, J. Jiang, and M. van Lier-Walqui, 2017a: An improved convective ice parameterization for the NASA GISS Global Climate Model and impacts on cloud ice simulation. *J. Climate*, **30**, no. 1, 317-336, doi:10.1175/JCLI-D-16-0346.1.

Elsaesser, G.S., C.W. O'Dell, M.D. Lebsock, R. Bennartz, and T.J. Greenwald, 2017b: The Multi-Sensor Advanced Climatology of Liquid Water Path (MAC-LWP). *J. Climate*, **30**, no. 24, 10193-10210, doi:10.1175/JCLI-D-16-0902.1.

Elsaesser, G. S., Roca, R., Fiolleau, T., Del Genio, A. D., & Wu, J. (2022). A simple model for tropical convective cloud shield area growth and decay rates informed by geostationary IR, GPM, and Aqua/AIRS satellite data. *Journal of Geophysical Research: Atmospheres*, **127**, e2021JD035599. https://doi.org/10.1029/2021JD035599.

Field P. R. and R. Wood, 2007: Precipitation and cloud structure in midlatitude cyclones. J. Climate, 20, 233-254, doi:10.1175/JCLI3998.1.

Gelaro, R., McCarty, W., Suarez, M. J., Todling, R., Molod, A., Takacs, L., … Zhao, B. (2017). The Modern-Era Retrospective Analysis for Research and Applications, Version 2 (MERRA-2). *J. Climate*, **30**(**14**), 5419–5454.

Gettelman, A. and Morrison, H., 2015: Advanced Two-Moment Bulk Microphysics for Global Models. Part I: Off-Line Tests and Comparison with Other Schemes, J. Climate, 28, 1268–1287, https://doi.org/10.1175/JCLI-D-14-00102.1.

Grim J. A., R. M. Rauber, M. K. Ramamurthy, B. F. Jewett and M. Han, 2007: High-resolution observations of the Trowal-Warm-frontal region of two continental winter cyclones. Month. Weath. Rev., 135, 1629-1646, doi:10.1175/MWR3378.1.

Han M., R. M. Rauber, M. K. Ramamurthy, B. F. Jewett and J. A. Grim, 2007: Mesoscale dynamics of the TROWAL and warm-frontal regions of two continental winter cyclones. Month. Weath. Rev. 135, 1647-1670, doi: 10.1175/MWR3377.1.

Hawcroft M. K., L. C. Shaffrey, K. I. Hodges and H. F. Dacre, 2012: How much northern hemisphere precipitation is associated with extratropical cyclones? Geophys. Res. Lett., 39, L24809, doi:10.1029/2012GL053866.

Hoskins B. J. and K. I. Hodges, 2002: New perspectives on the Northern Hemisphere winter storm tracks. J. Atmos. Sci., 59, 1041–1061.

Illingworth A. J. and 28 co-authors, 2015: The EarthCARE satellite: the next step forward in global measurements of clouds, aerosols, precipitation and radiation. Bull. Amer. Meterol. Soc, 96, 1311-1332, doi: 10.1175/BAMS-D-12-00227.1.

Jewell, R., 1981: Tor Bergeron's first year in the Bergen school: Towards an historical appreciation. *In: Lilequist, G. H. (Ed.) Weather and Weather Maps: a volume dedicated to the memory of Tor Bergeron. Vol. 10, Contributions to current research in Geophysics., Springer*, 474–490.

Kelley, M., G.A. Schmidt, L. Nazarenko, S.E. Bauer, R. Ruedy, G.L. Russell, A.S. Ackerman, I. Aleinov, M. Bauer, R. Bleck, V. Canuto, G. Cesana, Y. Cheng, T.L. Clune, B.I. Cook, C.A. Cruz, A.D. Del Genio, G.S. Elsaesser, G. Faluvegi, N.Y. Kiang, D. Kim, A.A. Lacis, A. Leboissetier, A.N. LeGrande, K.K. Lo, J. Marshall, E.E. Matthews, S. McDermid, K. Mezuman, R.L. Miller, L.T. Murray, V. Oinas, C. Orbe, C. Pérez García-Pando, J.P. Perlwitz, M.J. Puma, D. Rind, A.

Romanou, D.T. Shindell, S. Sun, N. Tausnev, K. Tsigaridis, G. Tselioudis, E. Weng, J. Wu, and M.-S. Yao, 2020: GISS-E2.1: Configurations and climatology. *J. Adv. Model. Earth Syst.*, **12**, no. 8, e2019MS002025, doi:10.1029/2019MS002025.

Konsta, D., Dufresne, J.-L., Chepfer, H., Vial, J., Koshiro, T., Kawai, H., et al., 2022: Low-level marine tropical clouds in six CMIP6 models are too few, too bright but also too compact and too homogeneous. *Geophys. Res. Lett*., **49**, e2021GL097593. Doi:10.1029/2021GL097593

Kunkel K. E., D. R. Easterling, D. A. R. Kristovich, B. Gleason, L. Stoecker and R. Smith, 2012: Meteorological causes of the secular variations in observed extreme precipitation events for the conterminous United States. J. Hyrometeorol, 13, 1131-1141, doi:10.1175/JHM-D-11-0108.1.

Kunkel K. E. and 24 co-authors, 2013: Monitoring and understanding trends in extreme storms, Bull. Amer. Meteorol. Soc., 94, 499-514, doi: 10.1175/BAMS-D-11-00262.1.

Li, J.-L., G. Cesana, K.-M. Xu, M. Richardson, H. Takahashi, and J. Jiang, 2023: Comparisons of simulated radiation, surface wind stress and SST fields over tropical pacific by the GISS CMIP6 versions of global climate models with observations. *Environ. Res. Commun,* **5**, 015005.

Mace G. G., Q. Zhang, M. Vaughan, R. Marchand, G. Stephens, C. Trepte, and D. Winker, 2009: A description of hydrometeor layer occurrence statistics derived from the first year of merged CloudSat and CALIPSO data. *J. Geophys. Res.,* **114**, D00A26, doi:10.1029/2007JD008755

Mace, G. G., and Q. Zhang, 2014: The CloudSat radar-lidar geometrical profile product (RL-GeoProf): Updates, improvements, and selected results, J. Geophys. Res. Atmos., 119, doi:10.1002/ 2013JD021374.

Marciano C. G., G. M. Lackmann and W. A. Robinson, 2015: Changes in U.S. east coast cyclone dynamics with climate change. J. Climate, 28, 468-484, doi:10.1175/JCLI-D-14-00418.1.

Martin, J. E., 1998a: The structure and evolution of a continental winter cyclone. Part I: Frontal structure and the occlusion process. Mon. Wea. Rev., 126 (2), 303–328.

Martin, J.E., 1998b: The structure and evolution of a continental winter cyclone. Part II: Frontal forcing of an extreme snow event. *Mon. Wea. Rev*., 126 (**2**), 329–348.

Martin, J.E., 1999a: Quasi-geostrophic forcing of ascent in the occluded sector of cyclones and the trowal airstream. *Mon. Wea. Rev*., 127, 70–88.

Martin, J.E., 1999b: The separate roles of geostrophic vorticity and deformation in the mid-latitude occlusion process. *Mon. Wea. Rev*., 127, 2404–2418.

Nam C., S. Bony, J.-L. Dufresne and H. Chepfer, 2012: The 'too few, too bright' tropical low-cloud problem in CMIP5 models. Geophys. Res. Lett. 29(21), doi:10.1029/2012GL063421.

Naud, C.M, J.F. Booth, J. Jeyaratnam, L.J. Donner, C.J. Seman, M. Zhao, H. Guo, and Y. Ming, 2019: Extratropical cyclone clouds in the GFDL climate model: Diagnosing biases and the associated causes. *J. Climate*, **32**, 6685-6701, doi:10.1175/JCLI-D-19-0421.1.

Naud, C.M., P. Ghosh, J.E. Martin, G.S. Elsaesser, and D.J. Posselt, 2024: A CloudSat-CALIPSO view of cloud and precipitation in the occluded quadrants of extratropical cyclones. *Q. J. Roy. Meteorol. Soc.*, early on-line, doi:10.1002/qj.4648.

Naud, C.M., J. Jeyaratnam, J.F. Booth, M. Zhao, and A. Gettelman, 2020: Evaluation of modeled precipitation in oceanic extratropical cyclones using IMERG. *J. Climate*, **33**, no. 1, 95-113, doi:10.1175/JCLI-D-19-0369.1.

Naud, C.M., J.E. Martin, P. Ghosh, G.S. Elsaesser, and D.J. Posselt, 2023: Automated identification of occluded sectors in midlatitude cyclones: Method and some climatological applications. *Q. J. Roy. Meteorol. Soc.*, 149 1990-2010, doi:10.1002/qj.4491.

Penner, C., 1955: A three-front model for synoptic analyses. Quart. J. Roy. Meteor. Soc., 81 (347), 89–91.

Pfahl S. and H. Wernli, 2012: Quantifying the relevance of cyclones for precipitation extremes. J. Climate, 25, 6770-6780, doi:10.1175/JCLI-D-11-00705.1.

Posselt, D. J., and J. E. Martin, 2004: The Effect of Latent Heat Release on the Evolution of a Warm Occluded Thermal Structure., *Mon. Wea. Rev.*, **132**, 578-599.

Russotto, R.D., J.D.O. Strong, S.J. Camargo, A.H. Sobel, G. Elsaesser, M. Kelley, A.D. Del Genio, Y. Moon, and D. Kim, 2022: Improved representation of tropical cyclones in the NASA GISS-E3 GCM. *J. Adv. Model. Earth Syst.*, **14**, no. 1, e2021MS002601, doi:10.1029/2021MS002601.

Schmidt, G.A., D. Bader, L.J. Donner, G.S. Elsaesser, J.-C. Golaz, C. Hannay, A. Molod, R. Neale, and S. Saha, 2017: Practice and philosophy of climate model tuning across six U.S. modeling centers. *Geosci. Model Dev.*, **10**, 3207-3223, doi:10.5194/gmd-10-3207-2017.

Schultz, D.M., and G. Vaughan, 2011: Occluded fronts and the occlusion process: A fresh look at conventional wisdom. *Bull. Amer. Meteor. Soc*., 92 ***(4***), 443–466.

Sinclair V. A. and J. L. Catto, 2023: The relationship between extratropical cyclone intensity and precipitation in idealized current and future climates. Weather Clim. Dyn., 4, 567-589, doi: 10.5194/wcd-4-567-2023.

Smith, R. N. B., 1990: A scheme for predicting layer clouds and their water content in a general circulation model, Q. J. Roy. Meteor. Soc., 116, 435- 460, doi:10.1002/qj.49711649210.

Stephens G. L., D. G. Vane, R. J. Boain, G. G. Mace, K. Sassen, Z. Wang, A. J. Illingworth, E. J. O'Connor, W. B. Rossow, S. L. Durden, S. D. Miller, R. T. Austin, A. Benedetti, C. Mitrescu, and the CloudSat Science Team, 2002: The CloudSat mission and the A-TRAIN: A new dimension to space-based observations of clouds and precipitation. *Bull. Am. Meteorol. Soc*., **83**, 1771-1790.

Sutcliffe, R., 1947: A contribution to the problem of development. *Quart. J. Roy. Meteor. Soc.*, **73** (**317-318**), 370–383.

Winker D.M., M.A. Vaughan, A.H. Omar, Y. Hu, K.A. Powell, Z. Liu, W.H. Hunt, and S.A. Young, 2009: Overview of the CALIPSO Mission and CALIOP Data Processing Algorithms, *J. Atmos. Oceanic Technol*., **26**, 2310-2323.

Yettella, V., and J. E. Kay, 2017: How will precipitation change in extratropical cyclones as the planet warms? Insights from a large initial condition climate model ensemble. *Climate Dyn*., 49, 1765–1781, https://doi.org/10.1007/s00382-016-3410-2

Zhang Z. and B. A. Colle, 2017: Changes in extratropical cyclone precipitation and associated processes during the twenty-first century over Eastern North America and the Western Atlantic using a cyclone-relative approach. J. Climate, 30, 8633-8656, doi:10.1175/JCLI-D-16-0906.1.